

Improved estimation of cluster mass profiles from the cosmic microwave background

Jaiyul Yoo^{1*} and Matias Zaldarriaga^{1,2}

¹*Harvard-Smithsonian Center for Astrophysics, Harvard University, 60 Garden Street, Cambridge, MA 02138 and*

²*Jefferson Physical Laboratory, Harvard University, 17 Oxford Street, Cambridge, MA 02138*

We develop a new method for reconstructing cluster mass profiles and large-scale structure from the cosmic microwave background (CMB). By analyzing the likelihood of CMB lensing, we analytically prove that standard quadratic estimators for CMB lensing are unbiased and achieve the optimal condition only in the limit of no lensing; they become progressively biased and sub-optimal, when the lensing effect is large, especially for clusters that can be found by ongoing Sunyaev-Zel'dovich surveys. Adopting an alternative approach to the CMB likelihood, we construct a new maximum likelihood estimator that utilizes delensed CMB temperature fields based on an assumed model. We analytically show that this estimator asymptotically approaches the optimal condition as our assumed model is refined, and we numerically show that as we iteratively apply it to CMB maps our estimator quickly converges to the true model with a factor of ten less number of clusters than standard quadratic estimators need. For realistic CMB experiments, we demonstrate the applicability of the maximum likelihood estimator with tests against numerical simulations in the presence of CMB secondary contaminants. With significant improvement on the signal-to-noise ratio, our new maximum likelihood estimator can be used to measure the cluster-mass cross-correlation functions at different redshifts, probing the evolution of dark energy.

PACS numbers: 98.62.Sb, 98.70.Vc, 98.80.Es

I. INTRODUCTION

As the most distant observable sources, the cosmic microwave background (CMB) anisotropies provide a unique channel to probe the universe after the cosmological recombination epoch. In particular, weak gravitational lensing of the CMB can be used to map the matter distribution in the universe at higher redshift than weak lensing of faint background galaxies can ever achieve. Recent work [1, 2, 3, 4] has focused on measuring the lensing signature in the CMB by large-scale structure between the last scattering surface and the present universe, but relatively little attention has been paid to weak lensing of the CMB by clusters of galaxies.

The abundance of massive clusters is exponentially sensitive to the growth of the underlying matter distribution, and hence it has been recognized as a powerful probe of the evolution of dark energy (e.g., [5]). However, the constraining power as a cosmological probe can be only realized, if the cluster masses are accurately measured. To achieve this goal, many cluster surveys are designed to detect massive clusters and measure their mass using the Sunyaev-Zel'dovich (SZ) effect, and some of the planned surveys are already operational using the South Pole Telescope (SPT), and the Atacama Cosmology Telescope (ACT). Weak lensing of the CMB can be applied to the same clusters found in the SZ surveys without additional observations, providing independent measurements of their mass. Furthermore, the CMB provides the highest redshift source plane with precision measurements of its distance, which can be combined with galaxy weak lensing measurements of the same lensing clusters to obtain angular diameter distance ratio estimates that are independent of the mass distribution, substantially increasing the leverage to constrain cosmological parameters [6].

Gravitational lensing by clusters imprints a unique signature in the CMB anisotropies. On arcminute scales, the primordial CMB anisotropies decay exponentially due to the photon diffusion from the baryon-photon fluid around the recombination epoch [7], and to a good approximation the CMB can be considered as a pure temperature gradient on small scales. Based on this approximation, Seljak and Zaldarriaga [8] showed that clusters create dipole-like wiggles in the CMB temperature by remapping the otherwise smooth gradient field, and this unique feature can be used to isolate the lensing effect by clusters and to reconstruct the deflection angle, once the temperature gradient is separately measured on large scales. Vale, Amblard, and White [9] and Holder and Kosowsky [10] used N -body simulations to model realistic lensing clusters, and they found that the mass reconstruction for individual clusters is compromised, since it is hard to measure the large-scale temperature gradient accurately and secondary anisotropies in the CMB can partially mimic the lensing signature.

However, it has been realized that one can apply the same technique developed for reconstructing large-scale structure to clusters of galaxies, measuring the statistical properties of a sample of clusters. Unlike galaxy weak lensing, CMB anisotropies have no characteristic shape, even statistically, from which the deviation is a measure of the lensing effect. Gravitational lensing, however, gives rise to a deviation of the two-point correlation function of the CMB temperature anisotropies from statistical isotropy. The standard technique is to construct a lensing estimator that is quadratic in observed temperature anisotropies, measuring the correlation between different Fourier modes, which is directly proportional to the lensing effect [11].

This method is easy to implement in analyzing real data compared to the full likelihood analysis [12] and no separate measurement is required to obtain the large-scale temperature gradient. However, Maturi et al. [13] showed that standard quadratic estimators need a modification to be an unbiased es-

*Electronic address: jyoo@cfa.harvard.edu

timator in a region around massive clusters. Hu, DeDeo, and Vale [14] quantitatively demonstrated that standard quadratic estimators based on the linear approximation ignore higher-order terms in the lensing effect that coherently contribute to the lensing reconstruction, and hence the reconstruction is biased low when the lensing effect is large. Furthermore, they proposed modified quadratic estimators that remove the higher-order terms in violation of the linear approximation by low-pass filtering observed temperature fields, and they showed that the modified quadratic estimators recover cluster mass profiles with no significant bias. However, the cutoff scale of the low-pass filter is somewhat arbitrary and it depends on the lensing effect, which we want to measure with the estimators.

Here we develop a new maximum likelihood estimator for reconstructing cluster mass profiles and large-scale structure by analyzing the likelihood of CMB lensing. Our approach is similar in making full use of the likelihood information to one advocated by Hirata and Seljak [12]. While they derive an analytic expression for a maximum likelihood estimator, it is impractical to apply to a realistic problem, because the solution is too general and computationally expensive. However, our maximum likelihood estimator is different from theirs and it is easy to use in practice, because we adopt an alternative approach to setting up the likelihood: it takes a similar form of standard quadratic estimators and it approaches the optimal condition as it is iteratively applied to CMB maps. Furthermore, we show that our maximum likelihood estimator can reconstruct cluster mass profiles with a factor of ten less number of clusters than standard or modified quadratic estimators need.

The rest of the paper is organized as follows. We first derive a quadratic estimator, accounting for the telescope beam effect in Sec. II. This consideration makes a difference compared to the usual practice in the literature, where quadratic estimators are often applied to beam deconvolved CMB maps. In Sec. III we analytically show that the quadratic estimators are unbiased and optimal only when the lensing effect vanishes, and why the modified quadratic estimators outperform the standard quadratic estimators when the lensing effect is large. Based on this observation, we construct a delensed temperature field and derive a maximum likelihood estimator using the delensed temperature field. We demonstrate its applicability to realistic CMB experiments using numerical simulations in Sec. IV. We discuss the impact of the telescope beam and instrumental noise in the delensing process and we conclude in Sec. V.

In this paper we will only consider lensing estimators based on CMB temperature anisotropies, since the planned surveys are not yet sensitive to CMB polarization anisotropies on arcminute scales. However, it is straightforward to extend our formalism to lensing estimators based on CMB polarization anisotropies. Throughout the paper we assume a flat Λ CDM universe with the matter density parameter $\Omega_m h^2 = 0.127$, the baryon density parameter $\Omega_b h^2 = 0.0222$, the Hubble constant $h = 0.73$, the spectral index $n_s = 0.95$, the optical depth to the last scattering surface $\tau = 0.09$, and the primordial curvature perturbation amplitude $A_s = 2.5 \times 10^{-9}$

(corresponding to the matter power spectrum normalization $\sigma_8 = 0.75$), consistent with the recent cosmological parameter estimation (e.g., [15, 16, 17])

II. FORMALISM

Here we describe our notations for weak lensing of the CMB and derive a quadratic estimator for CMB lensing reconstruction.

A. Weak Lensing of the CMB

Gravitational lensing deflects light rays as they propagate through fluctuating gravitational fields, and the deflection vector $\mathbf{d}(\hat{\mathbf{n}})$ at the angular position $\hat{\mathbf{n}}$ on the sky is related to the line-of-sight projection of the gravitational potential ψ as $\mathbf{d}(\hat{\mathbf{n}}) = \hat{\nabla}\phi(\hat{\mathbf{n}})$, where the projected potential is

$$\phi(\hat{\mathbf{n}}) = -2 \int_0^{D_*} dD \frac{D_* - D}{DD_*} \psi(D\hat{\mathbf{n}}, D), \quad (1)$$

$\hat{\nabla}$ is the derivative with respect to $\hat{\mathbf{n}}$, and D_* is the comoving angular diameter distance to the last scattering surface. Here we have assumed a flat universe and $c \equiv 1$. The projected potential is further related to the convergence κ as $\hat{\nabla}^2\phi(\hat{\mathbf{n}}) = -2\kappa(\hat{\mathbf{n}})$.

Since gravitational lensing conserves the surface brightness of diffuse backgrounds, the lensed temperature field $\tilde{T}(\hat{\mathbf{n}})$ of the CMB is simply the intrinsic (unlensed) temperature field $T(\hat{\mathbf{n}})$ remapped by the deflection vector,

$$\tilde{T}(\hat{\mathbf{n}}) = T \left[\hat{\mathbf{n}} + \hat{\nabla}\phi(\hat{\mathbf{n}}) \right]. \quad (2)$$

We will use notation with (or without) tilde to represent lensed (or unlensed) quantities. Note that we mainly work in the Rayleigh-Jeans tail and express the surface brightness in terms of temperature.

In a sufficiently small patch of the sky, it significantly simplifies the manipulations to work in Fourier space [see 18, 19, 20, for all-sky formalism]. In Fourier space the lensed temperature is

$$\begin{aligned} \tilde{T}_1 &= \int d^2\hat{\mathbf{n}} \tilde{T}(\hat{\mathbf{n}}) e^{-i\hat{\mathbf{l}}\cdot\hat{\mathbf{n}}} \\ &= T_1 - \int \frac{d^2\mathbf{l}'}{(2\pi)^2} [(1 - \mathbf{l}') \cdot \mathbf{l}'] T_{1'} \phi_{1-\mathbf{l}'} + \dots, \end{aligned} \quad (3)$$

where we Taylor expanded \tilde{T}_1 to the first order in ϕ_1 . We kept the same notation for Fourier components, while the functional dependence is indicated as a subscript (e.g., $T(\hat{\mathbf{n}})$)

and T_l are Fourier counterparts). The rms deflection angle $\langle \mathbf{d} \cdot \mathbf{d} \rangle^{1/2}$ is a few arcminutes and the deflection power peaks at a few degree scale, comparable to the angular sizes of clusters. However, the large-scale deflection field is coherent over the scales of the temperature fluctuations, resulting in an unobservable overall shift of the temperature field [21], and the linear approximation remains valid. In Sec. III we discuss the limitation of this approximation when the lensing effect is large in a region around massive clusters.

Since the intrinsic CMB is Gaussian and isotropic, the statistical properties of the temperature field can be completely described by the power spectrum C_l ,

$$\langle T_{l_1} T_{l_2}^* \rangle = (2\pi)^2 \delta(l_1 - l_2) C_{l_1}, \quad (4)$$

where the asterisk represents complex conjugation and δ is the Dirac delta function. Analogously, we define the projected potential power spectrum $C_l^{\phi\phi}$. Thus the deflection and the convergence power spectra are $C_l^{dd} = l^2 C_l^{\phi\phi}$ and $C_l^{\kappa\kappa} = l^4 C_l^{\phi\phi}/4$, respectively. Note that $C_l^{\phi\phi}$ can always be defined in this way, though it may be an incomplete description of the statistical properties of the projected potential when ϕ_l is non-Gaussian. Finally, the power spectrum of the lensed temperature field is

$$\tilde{C}_l = [1 - l^2 R] C_l + \int \frac{d^2 l'}{(2\pi)^2} [(1 - l') \cdot l']^2 C_{l-l'} C_{l'}^{\phi\phi}, \quad (5)$$

where $R \equiv (1/4\pi) \int d\ln l l^4 C_l^{\phi\phi}$ is the half of the rms deflection angle [18, 22].

In practice, the observed temperature field has two additional contributions: detector noise independent of the signal, and telescope beam convolving the signals from different patches of the sky. We assume that the detector noise is white, so that the noise power spectrum is constant,

$$C_l^N \equiv \Delta_T^2 = \sigma_{\text{pix}}^2 \frac{4\pi f_{\text{sky}}}{N_{\text{pix}}}, \quad (6)$$

where σ_{pix} is the rms error in each pixel of the detector in units of μK , f_{sky} is the fraction of the survey area on the sky, and N_{pix} is the total number of detector pixels [23]. Convolution is simply a multiplication in Fourier space, and the beam factor for a simple Gaussian beam we consider is $B_l = \exp[-\frac{1}{2}l^2\sigma_b^2]$. The beam width σ_b is related to the full-width half-maximum (FWHM) as $\sigma_b = \theta_{\text{FWHM}}/\sqrt{8 \ln 2}$. The observed temperature field and its power spectrum are then

$$\tilde{T}_1^{\text{obs}} = \tilde{T}_1 e^{-\frac{1}{2}l^2\sigma_b^2} + T_1^N, \quad (7)$$

$$\tilde{C}_l^{\text{obs}} = \tilde{C}_l e^{-l^2\sigma_b^2} + C_l^N. \quad (8)$$

In reality, one needs to consider other contributions to \tilde{T}^{obs} , such as residual foregrounds, point radio sources, and CMB secondary anisotropies. We will only consider secondary contributions in Sec. IV C.

B. Quadratic Estimator

Here we consider a convergence estimator $\hat{\kappa}(\hat{\mathbf{n}})$ that is quadratic in the observed temperature field, accounting for telescope beam and detector noise.¹ We require that the estimator be unbiased when averaged over an ensemble of CMB maps, $\langle \hat{\kappa}(\hat{\mathbf{n}}) \rangle = \kappa(\hat{\mathbf{n}})$. With these conditions, the estimator takes the general form in Fourier space

$$\hat{\kappa}_{\mathbf{L}} = \frac{N_L}{2} \int \frac{d^2 \mathbf{l}_1}{(2\pi)^2} F(\mathbf{l}_1, \mathbf{l}_2) \tilde{T}_{\mathbf{l}_1}^{\text{obs}} \tilde{T}_{\mathbf{l}_2}^{\text{obs}}, \quad (9)$$

where $\mathbf{l}_2 = \mathbf{L} - \mathbf{l}_1$ and N_L is a normalization coefficient, which only depends on $L = |\mathbf{L}|$. The functional form of $F(\mathbf{l}_1, \mathbf{l}_2)$ can be obtained by minimizing the variance of $\hat{\kappa}_{\mathbf{L}}$ and imposing the normalization condition

$$F(\mathbf{l}_1, \mathbf{l}_2) = \frac{[\mathbf{L} \cdot \mathbf{l}_1 C_{l_1} + \mathbf{L} \cdot \mathbf{l}_2 C_{l_2}]}{2 \tilde{C}_{l_1}^{\text{obs}} \tilde{C}_{l_2}^{\text{obs}}} e^{-\frac{1}{2}l_1^2\sigma_b^2} e^{-\frac{1}{2}l_2^2\sigma_b^2}, \quad (10)$$

and the normalization coefficient is

$$\frac{1}{N_L} = \frac{1}{L^2} \int \frac{d^2 \mathbf{l}_1}{(2\pi)^2} \frac{[\mathbf{L} \cdot \mathbf{l}_1 C_{l_1} + \mathbf{L} \cdot \mathbf{l}_2 C_{l_2}]^2}{2 \tilde{C}_{l_1}^{\text{obs}} \tilde{C}_{l_2}^{\text{obs}}} e^{-l_1^2\sigma_b^2} e^{-l_2^2\sigma_b^2}. \quad (11)$$

Finally, the variance of the estimator is

$$\langle \hat{\kappa}_{\mathbf{L}} \hat{\kappa}_{\mathbf{L}'}^* \rangle = (2\pi)^2 \delta(\mathbf{L} - \mathbf{L}') (C_L^{\kappa\kappa} + N_L^{\kappa\kappa}), \quad (12)$$

where $N_L^{\kappa\kappa} = L^2 N_L/4$ is the noise power spectrum of $\hat{\kappa}_{\mathbf{L}}$. One can think of $C_L^{\kappa\kappa}/N_L^{\kappa\kappa}$ as a signal-to-noise ratio, and the reconstruction becomes difficult at the angular scale L , where $C_L^{\kappa\kappa} \simeq N_L^{\kappa\kappa}$. Given experimental specifications, the noise power spectrum $N_L^{\kappa\kappa}$, as a function of the intrinsic CMB power spectrum C_L , becomes smallest, when there exists substantial power in C_L at the scale of interest, with its shape deviating from the scale-invariance ($L^2 C_L = \text{constant}$) [24].

¹ We will use quantities with hat to represent estimators of the quantities without hat, e.g., a convergence estimator is denoted as $\hat{\kappa}$ and a true convergence field is denoted as κ . However, this notational convention should not be confused with that used for temperature fields: T , \tilde{T} , \tilde{T}^{obs} , and \hat{T} represent the intrinsic (unlensed), the lensed [Eq. (2)], the observed [Eq. (7)], and the delensed [Eq. (27)] temperature fields, respectively.

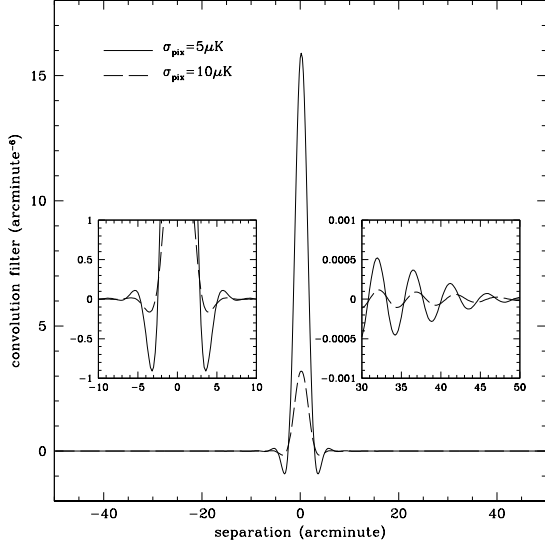


FIG. 1: Convolution filter $H(\theta)$ as a function of separation $\theta = |\hat{\mathbf{n}}|$ for CMB experiments with $\sigma_{\text{pix}} = 5\mu\text{K}$ and $10\mu\text{K}$ in Sec. IV. The insets show details of $H(\theta)$ at the center (*left*) and its tail (*right*).

Our estimator recovers the general form of the standard quadratic estimators as $\sigma_b \rightarrow 0$, and N_L corresponds to the noise power spectrum of a deflection estimator $\hat{\mathbf{d}}_L = 2\mathbf{L} \hat{\kappa}_L / L^2$ used in the literature [11].

The estimator can be decomposed as two Wiener-filtered temperature functions in real space, which essentially correlates the gradient of the lensed temperature field with the unlensed temperature field to isolate the lensing effect,

$$\mathbf{G}(\hat{\mathbf{n}}) = \int \frac{d^2\mathbf{l}}{(2\pi)^2} i\mathbf{l} \tilde{T}_1^{\text{obs}} \frac{C_l}{\tilde{C}_l^{\text{obs}}} e^{-\frac{1}{2}l^2\sigma_b^2 + i\mathbf{l}\cdot\hat{\mathbf{n}}} \quad (13)$$

$$W(\hat{\mathbf{n}}) = \int \frac{d^2\mathbf{l}}{(2\pi)^2} \tilde{T}_1^{\text{obs}} \frac{1}{\tilde{C}_l^{\text{obs}}} e^{-\frac{1}{2}l^2\sigma_b^2 + i\mathbf{l}\cdot\hat{\mathbf{n}}}, \quad (14)$$

and the convergence estimator can be expressed in terms of $\mathbf{G}(\hat{\mathbf{n}})$ and $W(\hat{\mathbf{n}})$ as

$$\hat{\kappa}_L = -\frac{N_L}{2} i\mathbf{L} \cdot \int d^2\hat{\mathbf{n}} \mathbf{G}(\hat{\mathbf{n}}) W(\hat{\mathbf{n}}) e^{-i\mathbf{L}\cdot\hat{\mathbf{n}}}. \quad (15)$$

This approach of using the two Wiener-filtered functions is more convenient for computing $\hat{\kappa}_L$ by using Fast Fourier Transform (FFT) routines than by directly computing Eq. (9). Furthermore, it is more physically intuitive than the general derivation, though the latter has clear advantage in its transparency and understanding the uniqueness of the functional form $F(\mathbf{l}_1, \mathbf{l}_2)$. A modified quadratic estimator can be constructed by removing the signals in Eq. (13) at $l \geq l_{\text{cut}}$, while Eq. (14) remains unchanged.

To better understand how quadratic estimators operate, we Fourier transform and rearrange Eq. (15) as

$$\begin{aligned} \frac{1}{2} \hat{\nabla} \cdot [\mathbf{G}(\hat{\mathbf{n}}) W(\hat{\mathbf{n}})] &= \int \frac{d^2\mathbf{L}}{(2\pi)^2} \frac{-\hat{\kappa}_L}{N_L} e^{i\mathbf{L}\cdot\hat{\mathbf{n}}} \quad (16) \\ &= \int d^2\hat{\mathbf{m}} H(\hat{\mathbf{m}} - \hat{\mathbf{n}}) \hat{\kappa}(\hat{\mathbf{m}}). \end{aligned}$$

The divergence of the two Wiener-Filtered functions is a convolution of the convergence estimate $\hat{\kappa}(\hat{\mathbf{n}})$ and the filter

$$H(\hat{\mathbf{n}}) = \int \frac{d^2\mathbf{L}}{(2\pi)^2} \frac{-1}{N_L} e^{i\mathbf{L}\cdot\hat{\mathbf{n}}}. \quad (17)$$

Figure 1 plots the filter $H(\theta)$ as a function of separation $\theta = |\hat{\mathbf{n}}|$ for experiments with $\sigma_{\text{pix}} = 5\mu\text{K}$ and $10\mu\text{K}$, to which we apply quadratic estimators in Sec. IV. The filter peaks at the center and its width is $\simeq 3'$, roughly set by the scale that the intrinsic CMB and detector noise power spectra become comparable. While the filter is highly oscillating at its tail, it is negligible at $\theta \geq 10'$ due to the large weight near the center. A factor of two change in σ_{pix} has little impact on the width of the filter, because the crossing scale is already at the CMB damping tail.

III. MAXIMUM LIKELIHOOD ESTIMATOR

In this section, we analyze the likelihood of CMB lensing by singular isothermal clusters. We first derive a quadratic estimator for singular isothermal clusters and compare the estimator to the optimal estimator from the likelihood. With the simple singular isothermal model, our analysis will be carried out analytically, showing that (1) the standard quadratic estimators are unbiased and optimal in the limit of no lensing, (2) they progressively become biased and sub-optimal when the lensing effect increases, and (3) why the modified quadratic estimators perform better than the standard quadratic estimators. Finally, we develop a unbiased maximum likelihood estimator to reconstruct cluster mass profiles as well as large-scale structure. We demonstrate its applicability to CMB experiments with tests against numerical simulations using more realistic cluster models in Sec. IV.

A. Quadratic Estimator for a Singular Isothermal Cluster

A singular isothermal cluster has a density profile $\rho(r) \propto r^{-2}$ and its enclosed mass increases with r , which requires truncation at some radius to be a viable model for real clusters. However, this model has advantage in its simplicity: its properties are described by one parameter, Einstein radius

$$\theta_E = 4\pi\sigma^2 \frac{D_* - D_L}{D_*}, \quad (18)$$

where σ is one-dimensional velocity dispersion of a cluster and D_L is the comoving angular diameter distance to the lensing cluster. CMB lensing has a well-defined single plane of the source redshift and the comoving angular diameter distance to the last scattering surface $D_* = 14.12$ Gpc is now measured with less than 1% uncertainty [17]. The convergence is $\kappa(\hat{\mathbf{n}}) = \theta_E/2\theta$ and the deflection vector is $\mathbf{d}(\hat{\mathbf{n}}) = -\theta_E\hat{\mathbf{n}}$ given the angular separation $\theta = |\hat{\mathbf{n}}|$ from the origin in a cluster centric coordinate. When a virial radius R_{vir} is defined as the radius inside which the mean density is 200 times the cosmic mean matter density, a singular isothermal cluster of mass $M = 10^{14}h^{-1}M_\odot$ within the virial radius at $z_L = 1$ has an Einstein radius $\theta_E = 8''.0$ and a velocity dispersion $\sigma = 2.0 \times 10^{-3}$ ($= 610 \text{ km s}^{-1}$), and they scale as $\theta_E \propto M^{2/3}$ and $\sigma \propto M^{1/3}$.

A quadratic estimator $\hat{\theta}_E^{\text{QE}}$ for singular isothermal clusters can be readily derived using the method described in Sec. II B, but here we take an idealized approach for the purpose of comparison, where we assume $\sigma_{\text{pix}} = \sigma_b = 0$. Under the condition that the estimator is unbiased $\langle \hat{\theta}_E^{\text{QE}} \rangle = \theta_E$ and it has the minimum variance, the quadratic estimator is

$$\hat{\theta}_E^{\text{QE}} = \frac{1}{\mathcal{F}} \int \frac{d^2\mathbf{l}_1}{(2\pi)^2} \int \frac{d^2\mathbf{l}_2}{(2\pi)^2} \times \frac{\tilde{T}_1 \tilde{T}_2 \pi(\mathbf{l}_1 C_{l_1} + \mathbf{l}_2 C_{l_2}) \cdot (\mathbf{l}_1 + \mathbf{l}_2)}{\tilde{C}_{l_1} \tilde{C}_{l_2} |\mathbf{l}_1 + \mathbf{l}_2|^3}, \quad (19)$$

with the normalization coefficient

$$\mathcal{F} = \int \frac{d^2\mathbf{l}_1}{(2\pi)^2} \int \frac{d^2\mathbf{l}_2}{(2\pi)^2} \times \frac{2\pi^2}{\tilde{C}_{l_1} \tilde{C}_{l_2}} \left[\frac{(\mathbf{l}_1 C_{l_1} + \mathbf{l}_2 C_{l_2}) \cdot (\mathbf{l}_1 + \mathbf{l}_2)}{|\mathbf{l}_1 + \mathbf{l}_2|^3} \right]^2. \quad (20)$$

The variance of the estimator is $\langle (\hat{\theta}_E^{\text{QE}} - \theta_E)(\hat{\theta}_E^{\text{QE}} - \theta_E) \rangle = 1/\mathcal{F}$. Here we Taylor expanded \tilde{T}_1 and kept terms only to the first order in θ_E in deriving $\hat{\theta}_E^{\text{QE}}$.

B. Relation to the Optimal Estimator

The likelihood function $P(\tilde{T}|\theta_E^m)$ simply represents the probability that a singular isothermal model with θ_E^m can have the lensed temperature field $\tilde{T}(\hat{\mathbf{n}})$. Since the intrinsic CMB follows a Gaussian distribution and gravitational lensing only remaps the intrinsic CMB, the distribution of $\tilde{T}(\hat{\mathbf{n}})$ is also Gaussian and its statistical properties are fully described by the covariance matrix of $\tilde{T}(\hat{\mathbf{n}})$

$$\tilde{C}(\hat{\mathbf{n}}, \hat{\mathbf{n}}') = \langle \tilde{T}(\hat{\mathbf{n}})\tilde{T}(\hat{\mathbf{n}}') \rangle = \int \frac{d^2\mathbf{l}}{(2\pi)^2} \tilde{C}_l e^{i\mathbf{l} \cdot (\hat{\mathbf{n}} - \hat{\mathbf{n}}')}. \quad (21)$$

For convenience, we take a negative logarithm of $P(\tilde{T}|\theta_E^m)$ and call it likelihood,

$$\mathcal{L}(\tilde{T}|\theta_E^m) \equiv -\ln P(\tilde{T}|\theta_E^m) \quad (22)$$

$$= \frac{1}{2} \tilde{T}(\hat{\mathbf{n}}) \tilde{C}^{-1}(\hat{\mathbf{n}}, \hat{\mathbf{n}}'|\theta_E^m) \tilde{T}(\hat{\mathbf{n}}') + \frac{1}{2} \ln \det \tilde{C}(\theta_E^m),$$

where the summation over $\hat{\mathbf{n}}$ and $\hat{\mathbf{n}}'$ is implicitly assumed and hereafter we will suppress the angular dependence for simplicity. In general, the likelihood is a functional with its argument of a scalar field, such as $\kappa(\hat{\mathbf{n}})$ or $\phi(\hat{\mathbf{n}})$. However, in our case it reduces to a function with its argument of a scalar θ_E^m , substantially simplifying the manipulation.

We take a derivative of \mathcal{L} with respect to θ_E^m ,

$$\frac{\partial \mathcal{L}}{\partial \theta_E^m} = -\frac{1}{2} \tilde{T} \tilde{C}^{-1} \frac{\partial \tilde{C}}{\partial \theta_E^m} \tilde{C}^{-1} \tilde{T} \quad (23)$$

$$= -\int \frac{d^2\mathbf{l}_1}{(2\pi)^2} \int \frac{d^2\mathbf{l}_2}{(2\pi)^2} \frac{\tilde{T}_1 \tilde{T}_2 \pi(\mathbf{l}_1 C_{l_1} + \mathbf{l}_2 C_{l_2}) \cdot (\mathbf{l}_1 + \mathbf{l}_2)}{\tilde{C}_{l_1} \tilde{C}_{l_2} |\mathbf{l}_1 + \mathbf{l}_2|^3},$$

where we computed the derivative to the first order in θ_E^m . Since gravitational lensing only redistributes the intrinsic CMB, the last term (log determinant) in Eq. (22) is independent of θ_E^m and hence the derivative with respect to θ_E^m vanishes in Eq. (23). However, in the presence of non-white instrumental noise, and/or other secondary contaminants, the derivative acquires a nonzero value but it is in general negligible compared to the quadratic term in Eq. (23). We will neglect this effect in the remainder of this paper. In the presence of significant contaminants from secondaries, the assumption that the likelihood function is Gaussian becomes invalid before the log determinant term becomes non-negligible.

With the derivative of \mathcal{L} , we can compute the Fisher information matrix

$$\mathcal{F} = \left\langle \frac{\partial^2 \mathcal{L}}{\partial \theta_E^{m2}} \right\rangle = \left\langle \frac{\partial \mathcal{L}}{\partial \theta_E^m} \frac{\partial \mathcal{L}}{\partial \theta_E^m} \right\rangle \quad (24)$$

where for the second equality we used the normalization condition of the likelihood function $1 = \int d\tilde{T} P(\tilde{T}|\theta_E^m) = \int d\tilde{T} e^{-\mathcal{L}}$. Within the Gaussian approximation, \mathcal{F} can be evaluated at any value of θ_E^m . Note that \mathcal{F} is identical to the normalization coefficient in Eq. (20).

In statistical parameter estimation, there exists a powerful theorem, known as the Cramér-Rao inequality that error bars in a parameter estimation have a definite lower bound $\sigma(\theta_E^m) \geq \mathcal{F}^{-1/2}$ set by the Fisher matrix. Moreover, this theorem provides a necessary and sufficient condition for an estimator to saturate the Cramér-Rao inequality, i.e., to be an optimal estimator $\hat{\theta}_E^{\text{opt}}$ [25],

$$\frac{\partial \mathcal{L}}{\partial \theta_E^m} = \mathcal{F}(\theta_E^m - \hat{\theta}_E^{\text{opt}}). \quad (25)$$

Now it is apparent that only in the limit of no lensing (the true Einstein radius $\theta_E = \theta_E^m = 0$) does the quadratic estimator $\hat{\theta}_E^{\text{QE}}$ become an optimal estimator $\hat{\theta}_E^{\text{opt}}$ with the smallest variance attainable from the data. Conversely, $\hat{\theta}_E^{\text{QE}}$ becomes progressively biased and sub-optimal as the lensing effect increases. This can be also understood by the validity of the linear approximation: since the quadratic estimator is constructed to be unbiased and to minimize the variance when \tilde{T}_1 is expanded to the linear order in ϕ_1 , it is natural to expect that this condition breaks down when higher-order terms in ϕ_1 become dominant over the linear order term. The modified quadratic estimator, on the other hand, removes the angular modes of the signals at $l \geq l_{\text{cut}}$ by explicitly setting the integrand zero in Eq. (19), where the linear approximation breaks down, and this process helps suppress the contributions from the higher-order terms in ϕ_1 because the higher-order terms are related to multiple integrals over the modes that are suppressed most. Precisely for this reason could the modified quadratic estimators be more robust than the standard quadratic estimators even when the lensing effect is large.

However, the modified quadratic estimator requires a rather arbitrary choice of the cutoff scale l_{cut} , which depends on the lensing effect, though it may be possible to calibrate against simulations [14]. Furthermore, the removal of the lensing signals at $l \geq l_{\text{cut}}$ inevitably results in lower signal-to-noise ratio, making the reconstruction noisier. We discuss this issue with numerical simulations in Sec. IV B.

C. Maximum Likelihood Estimator

Given the Gaussian probability distribution of the CMB, the likelihood retains all the information of the observed data. Even when there exists no optimal estimator, one can always find an estimator, if not analytically, that maximizes the likelihood: the maximum likelihood estimator $\hat{\theta}_E^{\text{ML}}$ is the solution of

$$\left. \frac{\partial \mathcal{L}}{\partial \theta_E^m} \right|_{\theta_E^m = \hat{\theta}_E^{\text{ML}}} = 0. \quad (26)$$

However, this equation is highly non-linear in general and requires approximations to be solved even numerically. Equations (25) and (26) show that an optimal estimator is always the maximum likelihood estimator. However, note that while the converse is not true in general, the maximum likelihood estimator asymptotically approaches to the optimal condition.

Having understood that the quadratic estimator becomes an optimal (and maximum likelihood) estimator in the limit of no lensing in Sec. III B, we present an alternative approach to modeling the likelihood and derive a new maximum likelihood estimator for singular isothermal clusters. We then gen-

eralize this approach to clusters with arbitrary mass distributions.

Consider a model with θ_E^m and its deflection field $\mathbf{d}^m(\hat{\mathbf{n}}) = -\theta_E^m \hat{\mathbf{n}}$. We construct a delensed temperature field $\hat{T}(\hat{\mathbf{n}})$ by delensing the observed $\tilde{T}(\hat{\mathbf{n}})$ with $\mathbf{d}^m(\hat{\mathbf{n}})$, and $\hat{T}(\hat{\mathbf{n}})$ is related to the intrinsic temperature field $T(\hat{\mathbf{n}})$ as

$$\begin{aligned} \hat{T}(\hat{\mathbf{n}}) &\equiv \tilde{T}(\hat{\mathbf{n}} - \mathbf{d}^m) \\ &= T(\hat{\mathbf{n}} - \mathbf{d}^m + \mathbf{d}) = T[(1 + \Delta)\hat{\mathbf{n}}], \end{aligned} \quad (27)$$

with $\Delta = \theta_E^m - \theta_E$. Now we can write the likelihood in terms of the delensed temperature field $\hat{T}(\hat{\mathbf{n}})$

$$\mathcal{L}(\hat{T}|\theta_E^m) = \frac{1}{2} \hat{T}(\theta_E^m) C^{-1} \hat{T}(\theta_E^m) + \frac{1}{2} \ln \det C, \quad (28)$$

where we emphasized the dependence of $\hat{T}(\hat{\mathbf{n}})$ on θ_E^m , and C is the covariance matrix of $T(\hat{\mathbf{n}})$. Taking a derivative of \mathcal{L} with respect to θ_E^m gives

$$\begin{aligned} \frac{\partial \mathcal{L}}{\partial \theta_E^m} &= \frac{1}{2} \left[\frac{\partial \hat{T}}{\partial \theta_E^m} C^{-1} \hat{T} + \hat{T} C^{-1} \frac{\partial \hat{T}}{\partial \theta_E^m} \right] \\ &= - \int \frac{d^2 \mathbf{l}_1}{(2\pi)^2} \int \frac{d^2 \mathbf{l}_2}{(2\pi)^2} \frac{T_{\mathbf{l}_1} T_{\mathbf{l}_2}}{C_{\mathbf{l}_1} C_{\mathbf{l}_2}} \frac{\pi(\mathbf{l}_1 C_{\mathbf{l}_1} + \mathbf{l}_2 C_{\mathbf{l}_2}) \cdot (\mathbf{l}_1 + \mathbf{l}_2)}{|\mathbf{l}_1 + \mathbf{l}_2|^3}. \end{aligned} \quad (29)$$

The second equality is obtained by evaluating the derivative at $\Delta = 0$. Assuming that our initial model with θ_E^* is a good approximation to the true model with θ_E ($\Delta_* = \theta_E^* - \theta_E \simeq 0$), the likelihood can be expanded around Δ_*

$$\begin{aligned} \mathcal{L} &= \mathcal{L}_* + \left(\frac{\partial \mathcal{L}}{\partial \theta_E^m} \right)_* (\Delta - \Delta_*) \\ &+ \frac{1}{2} \left(\frac{\partial^2 \mathcal{L}}{\partial \theta_E^{m2}} \right)_* (\Delta - \Delta_*)^2 + \mathcal{O}(\Delta^3), \end{aligned} \quad (30)$$

and we can use the standard Newton-Raphson method to solve Eq. (26) and obtain a maximum likelihood estimator $\hat{\theta}_E^{\text{ML}}$,

$$\begin{aligned} \Delta(\hat{\theta}_E^{\text{ML}}) - \Delta_* &= \hat{\theta}_E^{\text{ML}} - \theta_E^* \\ &= - \left(\frac{\partial \mathcal{L}}{\partial \theta_E^m} \right)_* \Big/ \left(\frac{\partial^2 \mathcal{L}}{\partial \theta_E^{m2}} \right)_*. \end{aligned} \quad (31)$$

It is important to note that the validity of our solution for $\hat{\theta}_E^{\text{ML}}$ is independent of the linear approximation, but the

convergence of $\hat{\theta}_E^{\text{ML}}$ depends on the goodness of θ_E^* to θ_E . Eq. (31) still involves computationally intensive evaluations of the second derivative, or the curvature matrix. We further simplify $\hat{\theta}_E^{\text{ML}}$ by replacing the curvature matrix with its ensemble average, Fisher matrix

$$\hat{\mathcal{F}} = \int \frac{d^2\mathbf{l}_1}{(2\pi)^2} \int \frac{d^2\mathbf{l}_2}{(2\pi)^2} \quad (32)$$

$$\times \frac{2\pi^2}{C_{l_1}C_{l_2}} \left[\frac{(\mathbf{l}_1 C_{l_1} + \mathbf{l}_2 C_{l_2}) \cdot (\mathbf{l}_1 + \mathbf{l}_2)}{|\mathbf{l}_1 + \mathbf{l}_2|^3} \right]^2,$$

and by evaluating the derivatives at $\Delta_\star = 0$. Finally, our new maximum likelihood estimator is

$$\hat{\theta}_E^{\text{ML}} = \theta_E^* + \frac{1}{\hat{\mathcal{F}}} \int \frac{d^2\mathbf{l}_1}{(2\pi)^2} \int \frac{d^2\mathbf{l}_2}{(2\pi)^2} \quad (33)$$

$$\times \frac{\hat{T}_{l_1} \hat{T}_{l_2}}{C_{l_1} C_{l_2}} \frac{\pi(\mathbf{l}_1 C_{l_1} + \mathbf{l}_2 C_{l_2}) \cdot (\mathbf{l}_1 + \mathbf{l}_2)}{|\mathbf{l}_1 + \mathbf{l}_2|^3}.$$

This equation is readily recognizable as the standard quadratic estimator in Eq. (19), except \tilde{C}_l and \tilde{T}_l replaced with C_l and \hat{T}_l . The resemblance should not be surprising, and in hindsight one could have expected this outcome given the result in Sec. III B: the quadratic estimator becomes optimal when the lensing effect is vanishingly small; as we delens $\tilde{T}(\hat{\mathbf{n}})$ well enough that $\hat{T}(\hat{\mathbf{n}})$ is close to $T(\hat{\mathbf{n}})$, the residual lensing effect in $\hat{T}(\hat{\mathbf{n}})$ is substantially reduced and therefore the maximum likelihood estimator takes the form of the quadratic estimator, returning diminishing change of the second term in Eq. (33), i.e., $\hat{\theta}_E^{\text{ML}} \simeq \theta_E^* \simeq \theta_E$.

We want to emphasize that this new estimator in the form of quadratic estimators is derived by iteratively solving for the maximum likelihood in Eq. (26) and updating the initial model θ_E^* as in the standard Newton-Raphson method, i.e., it is a maximum likelihood estimator and is independent of the linear approximation, to which the validity of the standard quadratic estimator is limited. One may be concerned about replacing the curvature matrix with the Fisher matrix in Eq. (33) and obtaining a solution quadratic in \hat{T}_l instead of a solution rational in \hat{T}_l (quadratic in \hat{T}_l both in numerator and in denominator). However, both procedures guarantee that the correct solution of Eq. (26) is iteratively found reaching the same peak of the likelihood, while the error estimation of parameters is approximated by using the Fisher matrix, rather than the full curvature matrix. In Sec. IV we demonstrate that this is a good approximation and the initial model converges quickly to the true model. Given the nomenclature of the existing quadratic estimators, now let us call our new maximum likelihood estimator an improved quadratic estimator.²

In practice we can use the standard quadratic estimators to obtain an initial model and then proceed with our improved quadratic estimator to refine the solution, even when the lensing effect is large. In general, the reconstruction of cluster mass profiles is too noisy to provide a good initial model. However, we can adopt an initial model for clusters from other observations (e.g., galaxy weak lensing and X-ray measurement) or theoretical expectations (e.g., Navarro-Frenk-White (NFW) profiles [26]). As opposed to the modified quadratic estimators, there is no arbitrary choice of l_{cut} in our method.

The toy model developed here can be readily generalized and our improved quadratic estimator can be used to reconstruct mass profiles of realistic clusters and large-scale structure. However, in the presence of the telescope beam and detector noise, the delensing process becomes non-optimal because it does not commute with the beam smoothing. In the absence of detector noise, one can deconvolve the beam factor, delens the temperature field, and convolve the beam again, which can solve the problem of non-commutativity.

However, in the presence of detector noise, the beam deconvolved noise can produce unwanted power on all scales when it is delensed due to the non-white power below the beam scale. One can in principle filter out or remove these small scales before delensing to mitigate the problem [14], which however introduces additional ad hoc scale to the problem. The impact of telescope beam and detector noise is small in practice for surveys like SPT ($\Delta_T \simeq 6\mu\text{K-arcmin}$) and ACT ($\Delta_T \simeq 10\mu\text{K-arcmin}$) as we numerically demonstrate in Sec. IV. We explicitly show in Appendix A that the delensing process suppresses the beam effect by a factor of the average magnification by clusters, since it corresponds to a mapping from the image plane to the source plane. Non-white instrumental noise and boundary effect of detectors may affect the delensing process. However, compared to the survey area, the lensing signals are limited to a relatively small region around clusters where none of those effect is expected to be significant.

IV. RECONSTRUCTING CLUSTER MASS PROFILES

Here we use numerical simulations of the CMB and cluster lensing potential to demonstrate the applicability of our improved quadratic estimator to CMB experiments. First, we adopt a more realistic model for massive clusters and investigate the dependence of our improved quadratic estimator on assumed initial models in Sec. IV A. Then we reconstruct cluster mass profiles using the standard, modified, and improved quadratic estimators, and we compare their performance in Sec. IV B. Finally, we discuss the effects of contaminants and investigate the robustness of our improved quadratic

iteration as an initial model, another iteration makes use of $\hat{T}(\hat{\mathbf{n}})$ that is constructed by using the initial model and this initial model is also a function of $\hat{T}(\hat{\mathbf{n}})$ in the previous iteration, which makes the estimator a rational function of temperature, instead of a quadratic function. Therefore, it is technically incorrect to call it a quadratic estimator.

² However, note that since our new estimator takes the result of the previous

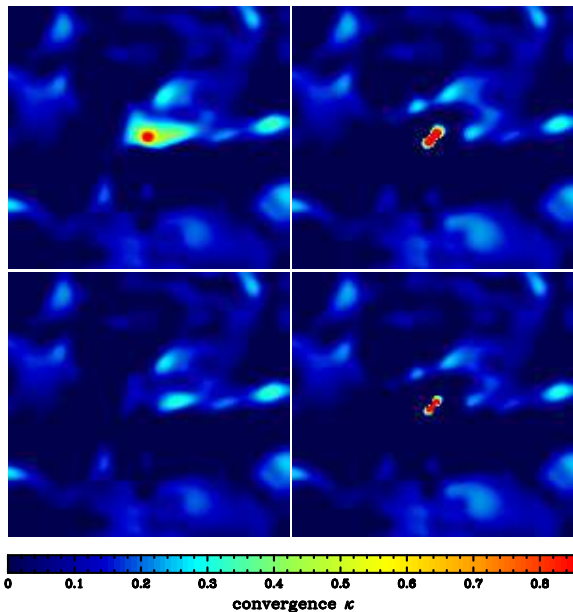


FIG. 2: (color online) Reconstructed convergence fields of a $30' \times 30'$ region around a cluster at $z_L = 1$ from an ideal experiment with $\Delta_T = 0$. Cluster mass is set $M = 5 \times 10^{14} h^{-1} M_\odot$. Improved quadratic estimators are applied once with initial mass models of $M_{\text{init}} = 5 \times 10^{14} h^{-1} M_\odot$ (left) and $M_{\text{init}} = 1 \times 10^{14} h^{-1} M_\odot$ (right) to a single patch of sky. The bottom panels show the residual after the true cluster convergence field is subtracted from the top panels.

estimators in the presence of the Sunyaev-Zel'dovich (SZ) effects.

A. Improved Quadratic Estimator

A singular isothermal model used in Sec. III is useful in developing an analytic solution of the likelihood approach. However, it is rather an academic model than a realistic model for massive clusters. Recent numerical simulations show that there exist a universal mass profile for dark matter halos, NFW profiles [26]

$$\rho(r) = \frac{\rho_s}{r/r_s(1+r/r_s)^2}. \quad (34)$$

The scale radius r_s is described by the concentration parameter $c = R_{\text{vir}}/r_s$ and the normalization coefficient ρ_s is related to the mass of clusters $M = 4\pi r_s^3 \rho_s [\ln(1+c) - c/(1+c)]$. We now use NFW profiles to model massive clusters.

The convergence field $\kappa(\hat{\mathbf{n}})$ of NFW profiles can be obtained by the ratio of the projected mass density $\Sigma(r)$ to the critical surface density Σ_{crit} of the lensing cluster at z_L ,

$$\kappa\left(\theta = \frac{r}{D_L}\right) = \frac{\Sigma(r)}{\Sigma_{\text{crit}}} = \frac{2 r_s \rho_s}{\Sigma_{\text{crit}}} P\left(\frac{r}{r_s}\right) (1+z_L)^2, \quad (35)$$

where the functional form $P(x)$ of the projected density is [27, 28]

$$\begin{aligned} P(x) &= \frac{1}{x^2-1} \left[1 - \frac{2}{\sqrt{1-x^2}} \tanh^{-1} \sqrt{\frac{1-x}{1+x}} \right], \quad (x < 1) \\ &= \frac{1}{3}, \quad (x = 1) \\ &= \frac{1}{x^2-1} \left[1 - \frac{2}{\sqrt{x^2-1}} \tan^{-1} \sqrt{\frac{x-1}{x+1}} \right], \quad (x > 1) \end{aligned} \quad (36)$$

and the critical surface density $\Sigma_{\text{crit}}^{-1} = 4\pi G D_L (D_\star - D_L)/D_\star(1+z_L)$ is only a function of z_L given the precise measurement of D_\star . Note that the convergence field κ of NFW profiles depend only on the angular separation $\theta = |\hat{\mathbf{n}}|$ due to spherical symmetry. The redshift dependence in Eq. (35) arises due to our use of comoving coordinates, reflecting higher densities of the universe at $z_L > 0$. For reference, $D_L = 850h^{-1}\text{Mpc}$ and $2400h^{-1}\text{Mpc}$, and $\Sigma_{\text{crit}} = 2.8 \times 10^3 h M_\odot \text{pc}^{-2}$ and $1.8 \times 10^3 h M_\odot \text{pc}^{-2}$ for $z_L = 0.3$ and 1, respectively. For clusters of $M = 5 \times 10^{14} h^{-1} M_\odot$ and $1 \times 10^{14} h^{-1} M_\odot$, $R_{\text{vir}} = 2.1h^{-1}\text{Mpc}$ and $1.2h^{-1}\text{Mpc}$ appear subtended by $3'.0$ and $4'.9$ on the sky at $z_L = 1$ and 0.3.

We use CMBFAST [29] to generate CMB temperature maps of $200' \times 200'$ (1000×1000 pixels) and set the pixel scale $0'.2$ smaller than detector beam sizes. Given a cluster mass M and redshift z_L , we first compute the convergence field $\kappa(\hat{\mathbf{n}})$ using Eq. (35). The lensing potential $\phi(\hat{\mathbf{n}})$ and its deflection vector $\mathbf{d}(\hat{\mathbf{n}})$ of the cluster are then computed in Fourier space, where their relations to $\kappa(\hat{\mathbf{n}})$ become a simple multiplication. The lensed temperature field $\tilde{T}(\hat{\mathbf{n}})$ is computed by displacing the intrinsic temperature field $T(\hat{\mathbf{n}})$ with $\mathbf{d}(\hat{\mathbf{n}})$ according to Eq. (2). Finally, we smooth $\tilde{T}(\hat{\mathbf{n}})$ with a telescope beam and add detector noises to obtain $\tilde{T}^{\text{obs}}(\hat{\mathbf{n}})$. Standard quadratic estimators can be used to reconstruct a convergence field $\hat{\kappa}(\hat{\mathbf{n}})$ by using Eqs. (13), (14), and (15) with $\tilde{T}^{\text{obs}}(\hat{\mathbf{n}})$, and so can modified quadratic estimators with a choice of l_{cut} , beyond which the integrand in Eq. (13) is set zero.

Similarly, our new estimation process begins with finding a solution $\hat{\mathbf{s}}$ to the delensing equation $\hat{\mathbf{s}} = \hat{\mathbf{n}} + \hat{\nabla} \phi^m(\hat{\mathbf{n}})$ given the lensing potential $\phi^m(\hat{\mathbf{n}})$ of an assumed initial model. We then construct a delensed temperature field $\hat{T}(\hat{\mathbf{s}}) = \tilde{T}^{\text{obs}}(\hat{\mathbf{n}})$ and use the same equations with $\tilde{T}^{\text{obs}}(\hat{\mathbf{n}})$ replaced by $\hat{T}(\hat{\mathbf{s}})$ to reconstruct $\hat{\kappa}_{\mathbf{L}}$. Imposing a consistency condition between the assumed model and the estimation result can provide a criterion for the iteration convergence of our improved quadratic estimators.

ACT and SPT will find $\sim 2 \times 10^4$ massive clusters mainly by the spectral distortion of the CMB arising from the inverse Compton scattering of hot electrons in clusters, so called the SZ effect [30, 31], with roughly redshift-independent threshold mass $M \geq 2 \times 10^{14} h^{-1} M_\odot$. To test our improved quadratic estimators, we consider a typical cluster of $M = 5 \times 10^{14} h^{-1} M_\odot$ and $c = 3$. Figure 2 shows the reconstructed $\hat{\kappa}(\hat{\mathbf{n}})$ of a massive cluster at $z_L = 1$ in an ideal

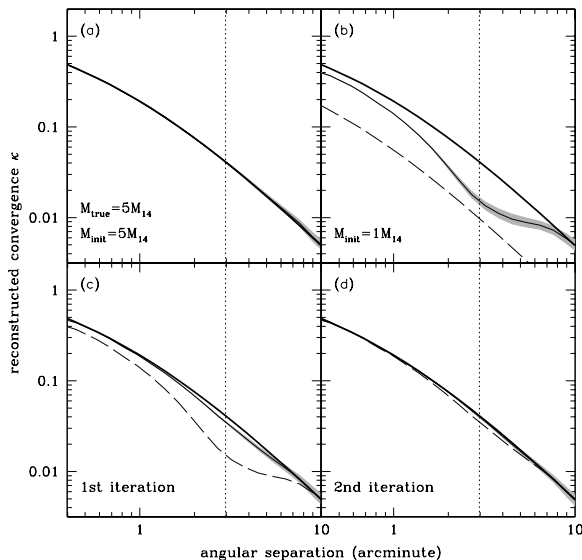


FIG. 3: Dependence of reconstructed mass profiles on an initial mass model M_{init} . Thick and thin solid lines represent the true cluster mass profile and the mean of reconstructed mass profiles from 500 clusters. The mass profiles are obtained by averaging reconstructed convergence over the annulus of each cluster. The uncertainties in the mean profile are shown as shaded regions. Dashed lines show an assumed initial mass model and the cluster virial radius is shown as vertical dotted lines. In Panels (c) and (d), the initial mass models are taken as the mean mass profile from the previous iteration. The reconstruction quickly converges to the true mass profile in two iterations even with an incorrect choice of $M_{\text{init}} = 1 \times 10^{14} h^{-1} M_{\odot}$, exhibiting no detectable bias in an ideal experiment.

experiment with $\Delta_T = 0$. Here we simply adopt a NFW profile with fixed concentration $c = 3$ for our initial model and allow mass M_{init} of the model to vary. Even with fixed concentration, r_s changes as a function of M_{init} , and hence our assumption allows for changes in the shape as well as the scaling of initial mass models. However, note that while we use this parametrized model of clusters, our reconstruction is general and non-parametric, such that we recover 2-D structure of $\kappa(\hat{\mathbf{n}})$ at each pixel rather than obtain model parameters M and c (see [32, 33] for reconstructing a parametrized cluster model). We assume that the cluster center is known from other observations with uncertainty less than our pixel scale 0.2 . The upper panels show the reconstructed $\hat{\kappa}(\hat{\mathbf{n}})$ from our improved quadratic estimator using an initial model of $M_{\text{init}} = 5 \times 10^{14} h^{-1} M_{\odot}$ (left) and $1 \times 10^{14} h^{-1} M_{\odot}$ (right), and the bottom panels show the residual after the true $\kappa(\hat{\mathbf{n}})$ is subtracted from the top panels.

With the perfect initial model in the left panels, the delensed temperature field $\hat{T}(\hat{\mathbf{n}})$ is identical to the intrinsic $T(\hat{\mathbf{n}})$, and our improved quadratic estimator returns *no* change on average to the initial model (bottom). However, there exist random noises in $\hat{\kappa}(\hat{\mathbf{n}})$ over the map, arising from the fluctuations of the intrinsic temperature gradient, though they are evidently small and discernible from the massive cluster (top). In the right panels, $\tilde{T}(\hat{\mathbf{n}})$ is delensed with the imperfect initial model, so that $\hat{T}(\hat{\mathbf{n}})$ is not identical to $T(\hat{\mathbf{n}})$ but the lensing

effect is significantly reduced. In this regime, quadratic estimators become asymptotically optimal and reconstruct $\kappa(\hat{\mathbf{n}})$ unbiased. The top panel exhibits small anisotropy and some residual remains in the bottom panel. In a single patchy of the sky, the CMB anisotropy has a gradient direction and gravitational lensing of the CMB makes no difference orthogonal to the gradient direction, in which reconstruction is completely degenerate, resulting in the asymmetry in $\hat{\kappa}(\hat{\mathbf{n}})$. However, since the CMB has no preferred direction, this obstacle can be overcome by stacking clusters in different patches of the sky. In practice, this stacking process provides the average $\kappa(\hat{\mathbf{n}})$ of the clusters, or the cluster-mass cross-correlation function [14]. Hereafter we assume that identical clusters are stacked for simplicity.

We now quantify the ability to reconstruct $\kappa(\hat{\mathbf{n}})$ with varying accuracy of assumed models. Figure 3 plots the reconstructed cluster mass profiles from 500 clusters (*thin solid*). The mass profiles are obtained by averaging reconstructed $\hat{\kappa}(\hat{\mathbf{n}})$ over the annulus of each cluster, and the uncertainties in the mean mass profile are shown as shaded regions. Figure 3a shows that our improved quadratic estimator is unbiased when our assumed model is perfect; it recovers the true model (*thick solid*) with no bias. If an assumed initial model is significantly different from the true model in Fig. 3b, the improved quadratic estimator suffers from the same problem that the standard quadratic estimators have, and the reconstruction is again biased low when the residual lensing effect is large. However, the reconstructed $\hat{\kappa}(\hat{\mathbf{n}})$ is inconsistent with our assumed model (*dashed*), implying that it has not converged to the correct solution. In Fig. 3c we take the reconstructed $\hat{\kappa}(\hat{\mathbf{n}})$ as a new initial model and apply our improved quadratic estimator to the same clusters. The reconstructed $\hat{\kappa}(\hat{\mathbf{n}})$ is now close to the true $\kappa(\hat{\mathbf{n}})$, but still inconsistent with the assumed model. We iterate once more in Fig. 3d and the reconstructed $\hat{\kappa}(\hat{\mathbf{n}})$ is identical to the true $\kappa(\hat{\mathbf{n}})$. One more iteration results in no further change and the estimate is consistent with the assumed and also the true models, indicating the convergence of our estimates.

Even with the imperfect initial model, the reconstruction quickly converges to the true $\kappa(\hat{\mathbf{n}})$ and no significant bias develops even beyond R_{vir} (*dotted*). When the reconstructed $\hat{\kappa}(\hat{\mathbf{n}})$ is inconsistent with the assumed model, one can in principle adopt a different initial model for a faster convergence before applying the estimator iteratively. Note that the asymmetry seen in Fig. 2 disappears and the reconstructed $\hat{\kappa}(\hat{\mathbf{n}})$ restores symmetry, once many clusters are stacked. Furthermore, the uncertainties in the mean profile decrease as our assumed model converges to the true model, because it solely results from the intrinsic fluctuations of the CMB in the case of perfect delensing.

B. Performance Comparison

Before we assess the performance of the three lensing estimators in realistic experiments, we first compare our improved quadratic estimator to the standard quadratic estimator, when the lensing effect is small. Figure 4 plots the re-

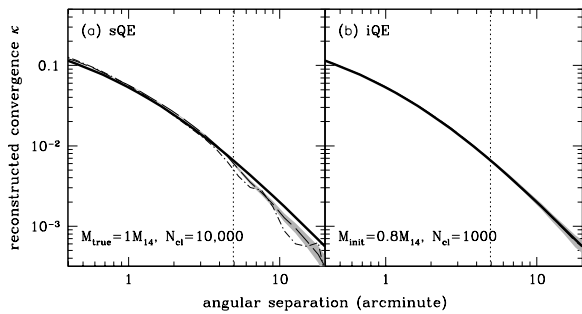


FIG. 4: Mass profile reconstruction for low mass clusters of $M = 1 \times 10^{14} h^{-1} M_{\odot}$ at $z_L = 0.3$ from standard (sQE) and improved (iQE) quadratic estimators (in the same format as in Fig. 3). 10,000 (left) and 1000 (right) clusters are used to obtain the mean profile, and the shaded region shows the uncertainties in the mean profile. Both estimators recover the true mass profiles within R_{vir} in the low mass regime. Approximately ten times more clusters are needed for sQE to achieve the same accuracy than for iQE. However, for comparison we plot the mean profile from 1000 clusters as the dot-dashed line in the left panel.

constructed cluster mass profiles in the same format as Fig. 3. For clusters of $M = 1 \times 10^{14} h^{-1} M_{\odot}$ at $z_L = 0.3$ ($\kappa \ll 1$), the improved quadratic estimator recovers the true mass profile with no detectable bias after two iterations. With signals smaller by a factor of five than in Fig. 3, 1000 clusters are stacked to obtain the mean mass profile, while 10,000 clusters are required for the standard quadratic estimator. As we quantify the difference in the signal-to-noise ratio below, the standard quadratic estimator needs approximately ten times as many clusters as the improved quadratic estimator needs to achieve the same accuracy, but we show the mean profile (dot-dashed) obtained by applying the standard quadratic estimator to 1000 clusters for comparison. Once enough clusters are stacked, the standard quadratic estimator works well within R_{vir} , though it shows some hint of deviation at the core. Thus, the standard quadratic estimator may be safely used to reconstruct mass profiles of clusters with $M < 1 \times 10^{14} h^{-1} M_{\odot}$ at $z_L = 0.3$. However, given the source of the CMB at $z_{\star} = 1090$, the lensing effect becomes larger as z_L increases, until Σ_{crit} reaches the minimum at $z_L \simeq 2.5$, where D_L becomes a half of D_{\star} . Therefore, the standard quadratic estimator cannot be used to reconstruct unbiased mass profiles of clusters that are either at $z_L \geq 0.3$ or massive $M \geq 1 \times 10^{14} h^{-1} M_{\odot}$. Since ACT and SPT will find clusters of $M \geq 2 \times 10^{14} h^{-1} M_{\odot}$ at higher redshift, modified or improved quadratic estimators are preferred to the standard quadratic estimator.

Now we consider realistic experiments with $\sigma_{\text{pix}} = 5 \mu\text{K}$ and compare the performance of the lensing estimators in Fig. 5. Since the reconstruction becomes noisier in the presence of detector noise and telescope beam, 10,000 clusters are stacked for the mean mass profiles when the standard or modified quadratic estimator is used, while the improved quadratic estimator is iteratively applied to only 1000 clusters. For clusters of $M = 5 \times 10^{14} h^{-1} M_{\odot}$ at $z_L = 1$, Fig. 5a shows that the standard quadratic estimators become substantially biased

in a region around massive clusters, consistent with the previous results [13, 14]. Quadratic terms in ϕ_1 ignored in the linear approximation coherently contribute to $\hat{\kappa}_1$, and hence the reconstructed $\hat{\kappa}(\hat{\mathbf{n}})$ is biased low where the linear approximation is violated [14].

Next we consider a modified quadratic estimator in Fig. 5b and adopt $l_{\text{cut}} = 1500$. The modified quadratic estimator recovers the true mass profile within R_{vir} but with small deviation beyond R_{vir} . The modified quadratic estimators operate in the same way of the standard quadratic estimators, except signals are removed on small scales ($l \geq l_{\text{cut}}$), where the linear approximation is violated. However, the choice of l_{cut} is rather arbitrary and should be calibrated against simulations: lower l_{cut} is needed for more massive clusters. Note that the modified quadratic estimator with $l_{\text{cut}} \rightarrow \infty$ exactly reduces to the standard quadratic estimator (in practice $l_{\text{cut}} \gtrsim 10^4$ can achieve this limit because of the Silk damping). In other words, a modified quadratic estimator with $l_{\text{cut}} \simeq 10^4$ fails to reconstruct the mass profile (born out by Fig. 5a). Moreover, we had to adopt $l_{\text{cut}} = 1500$ to reconstruct the mass profile in Fig. 5b and 5d, a more aggressive choice than $l_{\text{cut}} = 2000$ proposed in [14], with which we cannot recover the mass profile. This reflects the sensitivity of the modified quadratic estimator to l_{cut} as a function of cluster mass. Larger number of clusters are also required to reconstruct the true mean mass profile due to the reduction in the signal-to-noise ratio.

Figure 5c shows the reconstruction by our improved quadratic estimator with $M_{\text{init}} = 1 \times 10^{14} h^{-1} M_{\odot}$. The improved quadratic estimator recovers the true mass profile with no significant bias in the presence of detector noise. After a few iterations, the estimates quickly converge to the true model and the scatter around the mean is greatly reduced compared to Fig. 5b. Note that we iteratively applied the improved quadratic estimator to the same 1000 clusters.

In Fig. 5d and 5e, we consider the effect of telescope beam with $\theta_{\text{FWHM}} = 0'.5$. Both estimators in Fig. 5d and 5e recover the true mass profile unbiased in the presence of detector beam, while there exist some deviations in both cases. However, note that we explicitly account for the beam effect using the formulas developed in Sec. II B, rather than deconvolve the beam before applying the lensing estimators. The latter approach often used in the literature suffers from deconvolved detector noise exponentiating on small scales. This problem requires a low-pass filtering of reconstructed $\hat{\kappa}(\hat{\mathbf{n}})$, additionally removing the signals below the beam scale, which results in a distortion of its shape of $\hat{\kappa}(\hat{\mathbf{n}})$, making it hard to compare directly to theoretical predictions. However, in reality beam convolution suppresses detector noises (of course lensing signals as well), and it simply makes the reconstruction noisy below the beam scale. The dot-dashed line in Fig. 5d contrasts the reconstruction when we explicitly remove $\hat{\kappa}(\hat{\mathbf{n}})$ at $l \geq 1/\sigma_b$, where $\hat{\kappa}(\hat{\mathbf{n}})$ is obtained by applying the modified quadratic estimator with beam-deconvolved data (the line is displaced to avoid confusion with other lines). Significant shape distortion in $\hat{\kappa}(\hat{\mathbf{n}})$ complicates the interpretation.

For a larger beam size comparable to the scale radius of the clusters ($\theta_{\text{FWHM}} \simeq 1'$), the reconstruction becomes more challenging: modified quadratic estimators cannot recover the

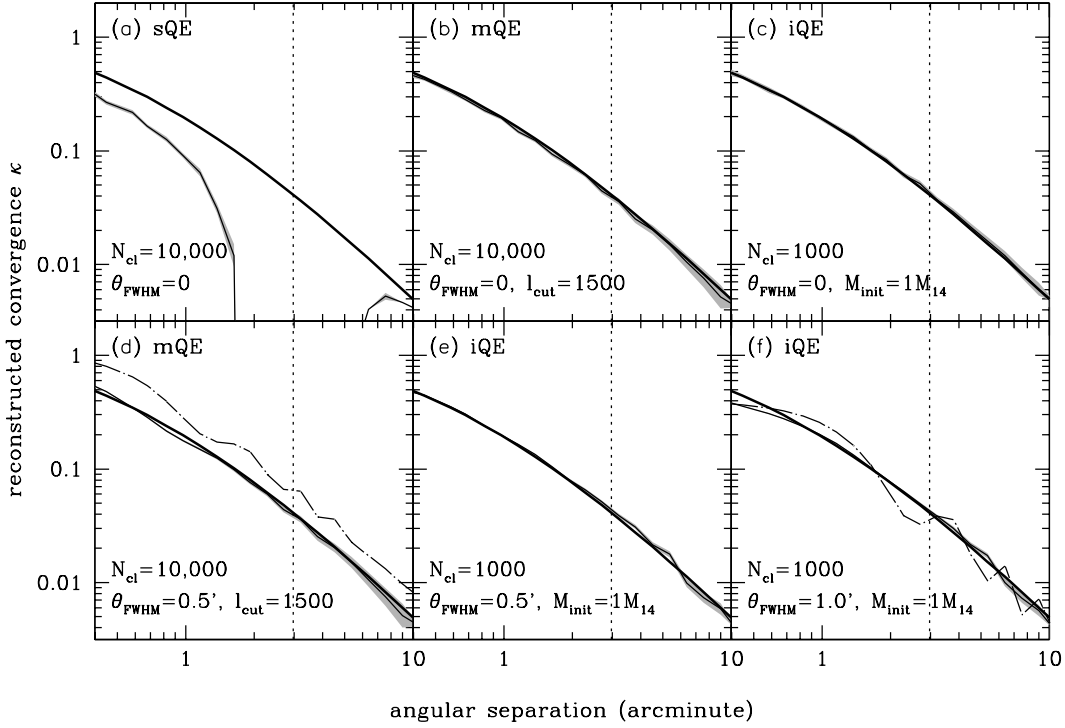


FIG. 5: Comparison of reconstructed mass profiles from standard (sQE), modified (mQE), and improved (iQE) quadratic estimators in realistic experiments with $\sigma_{\text{pix}} = 5\mu\text{K}$. The reconstruction is more difficult in the presence of detector noise and telescope beam. For the mean of reconstructed mass profiles, 10,000 clusters of $M = 5 \times 10^{14} h^{-1} M_{\odot}$ at $z_L = 1$ are stacked when sQE or mQE is used, while iQE is iteratively applied to only 1000 clusters. The shaded regions show the uncertainties in the mean profile. The dot-dashed line (panel d) shows the shape distortion in $\hat{\kappa}(\hat{\mathbf{n}})$ when mQE is applied after beam-deconvolution, and the line is displaced to avoid confusion (see the text). With $\theta_{\text{FWHM}} = 1'$ (panel f), iQE can recover the mean mass profile with small bias below the beam scale. For comparison, we plot the reconstructed mass profile (*dot-dashed*) using mQE in Panel (f).

cluster mass profile without significant shape distortion (*dot-dashed*). The improved quadratic estimator in Fig. 5f recovers the true mass profile beyond R_{vir} , while it develops small bias below the beam scale.

Figure 6 plots the fractional difference between the lensing estimates and the true cluster mass profile in Fig. 5, comparing their uncertainty in the mean profile. The difference (*lines*) is computed from the mean mass profiles by stacking 10,000 clusters for both estimators, while the statistical uncertainty (*gray bands*) in the difference is scaled for 500 clusters for comparison. The left panel shows that both estimators recover the cluster mass profile at the 5% level or better in the absence of telescope beam, while the modified quadratic estimator may need fine-tuning of l_{cut} to achieve better accuracy. However, the difference in their measurement uncertainty is in stark contrast: the improved quadratic estimator has a significantly higher signal-to-noise ratio than the modified quadratic estimator. While the reconstruction becomes harder especially beyond R_{vir} in the presence of telescope beam shown in the right panel, this trend of signal-to-noise ratio difference persists. Note that due to the beam smoothing effect the uncertainty in the estimates at $\theta \leq \theta_{\text{FWHM}}$ is reduced while it is highly correlated among adjacent bins.

So far we have numerically demonstrated the performance of the lensing estimators in Figs. 5 and 6: standard quadratic

estimators are significantly biased; modified and improved quadratic estimators recover the cluster mass profile with no bias, while they show substantial difference in the number of clusters that is required to obtain the mean mass profile. To quantify this difference, we evaluate $\Delta\chi^2$ of each lensing estimator

$$\Delta\chi^2 = \sum_{\theta, \theta'} \kappa(\theta) C_{\hat{\kappa}}^{-1}(\theta, \theta') \kappa(\theta'), \quad (37)$$

where the covariance matrix of $\hat{\kappa}(\theta)$ is

$$C_{\hat{\kappa}}(\theta, \theta') = \langle [\hat{\kappa}(\theta) - \kappa(\theta)] [\hat{\kappa}(\theta') - \kappa(\theta')] \rangle. \quad (38)$$

Since $\hat{\kappa}(\hat{\mathbf{n}})$ is computed from the two Wiener-filtered functions of the CMB temperature anisotropies, the covariance matrix is non-diagonal. The finite width of the convolution filter $H(\hat{\mathbf{n}})$ in Eq. (17) also reflects that the lensing estimators are a non-local function of the CMB temperature anisotropies, and hence non-zero $C_{\hat{\kappa}}$ when $\theta \neq \theta'$.

In the absence of telescope beam in Figs. 5b, 5c, and 6a, the ratio of $\Delta\chi^2$ for the modified quadratic estimator relative to the improved quadratic estimator is 8.1: a factor of eight larger

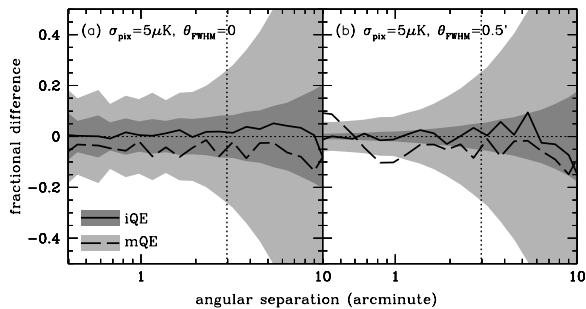


FIG. 6: Fractional difference between the lensing estimates and the true cluster mass profile in Fig. 5. The difference (*lines*) is computed from the mean mass profiles obtained by stacking 10,000 clusters for both estimators, while the statistical uncertainty (*gray bands*) in the difference is scaled for 500 clusters. The vertical dotted lines show the cluster virial radius.

number of clusters is required for the modified quadratic estimator to achieve the same level of accuracy than that for the improved quadratic estimator. In the presence of telescope beam in Figs. 5*d*, 5*e*, and 6*b*, beam smoothing substantially degrades the ability to recover the true cluster mass profile for both estimators, and its effect is relatively larger for the modified quadratic estimator, increasing the ratio to 10.4.

C. Sunyaev-Zel'dovich Effects

On small scales ($l > 2000$), the primordial CMB temperature anisotropies decay exponentially due to the Silk damping [7] and the dominant source of secondary anisotropies is the thermal Sunyaev-Zel'dovich (tSZ) effect, arising from scattering off hot electrons in massive clusters. However, the tSZ effect imprints a unique frequency dependence in the CMB temperature anisotropies, which in principle can be used to remove the tSZ signals. The same Compton scattering process also gives rise to a Doppler effect in the CMB temperature anisotropies due to the bulk motion of electron gas, or the kinetic Sunyaev-Zel'dovich (kSZ) effect (see [34, 35] for recent reviews). These kSZ signals, albeit smaller than tSZ signals, are spectrally indistinguishable from the intrinsic CMB temperature anisotropies, introducing an artifact in the lensing reconstruction. Here we assume that the tSZ signals can be cleaned perfectly, and we investigate how the kSZ signals deteriorate the lensing reconstruction.

For simplicity, we assume that the gas density traces the dark matter distribution in a massive cluster, with the same NFW profile. Given the line-of-sight velocity v_{los} of the cluster, the kSZ effect results in temperature anisotropies

$$\Delta T(\theta) = -v_{\text{los}} \tau(\theta) T_{\text{CMB}} \equiv -\Delta T_{\text{kSZ}} \frac{\Sigma(\theta)}{\Sigma(0)}, \quad (39)$$

where $\tau(\theta)$ is the Thompson scattering optical depth, proportional to the projected density $\Sigma(r = D_L \theta)$. We parametrized

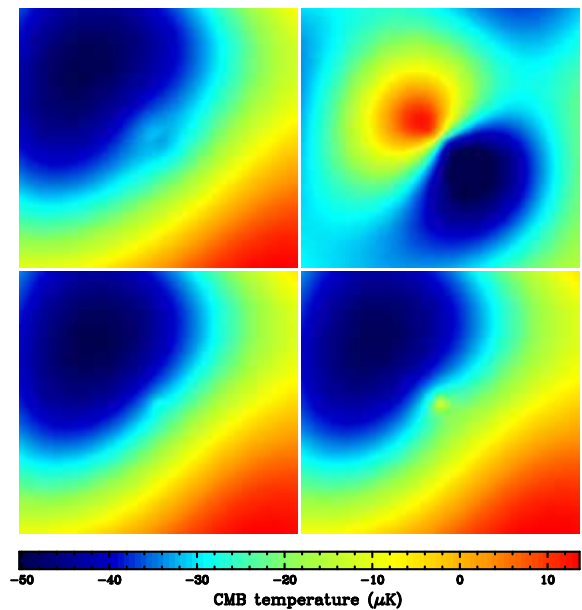


FIG. 7: (color online) Cluster lensing and kinetic Sunyaev-Zel'dovich (kSZ) effects on the CMB. For comparison, we plot $6' \times 6'$ regions of CMB temperature maps around a cluster of $M = 5 \times 10^{14} h^{-1} M_{\odot}$ ($\theta_{\text{vir}} = 3.0$) at $z_L = 1$. *Upper panels*: lensed temperature map (*left*) and its difference from the intrinsic temperature map (*right*). *Bottom panels*: assuming that the cluster is moving toward an observer, the kSZ effect is set $\Delta T_{\text{kSZ}} = 3$ (*left*) and $15 \mu\text{K}$ (*right*) at the center. The color scales in each panel represent the same temperature except in the upper right panel, where the color represents the difference ranging from $-5 \mu\text{K}$ to $5 \mu\text{K}$.

the product of v_{los} and $\tau(0)$ as ΔT_{kSZ} . Note that since the intrinsic CMB and kSZ induced anisotropies dilute in the same way as the universe expands, there is no $(1 + z_L)$ factor in Eq. (39) and $T_{\text{CMB}} = 2.725\text{K}$ is the CMB temperature today.

For a typical cluster with electron number density $\sim 0.01 \text{ cm}^{-3}$ and core radius $\sim 100 \text{ kpc}$, the Thompson scattering optical depth is $\tau(0) = 2 \times 10^{-3}$ at the core. The rms velocity dispersion in linear theory is $\sigma_v = 1.3 \times 10^{-3} (= 390 \text{ km s}^{-1})$ at $z_L = 1$, and this results in the rms temperature fluctuation $\Delta T_{\text{kSZ}} = 3.7 \mu\text{K}$ at the core. We randomly draw $\Delta T(0)$ from a Gaussian distribution with zero mean and dispersion $\sigma = \Delta T_{\text{kSZ}}$, then we add $\Delta T(\hat{n})$ to $\tilde{T}(\hat{n})$ for observations of each cluster.

First, we compare the cluster lensing and kSZ effects on the CMB temperature field. Figure 7 plots a $6' \times 6'$ regions of CMB maps around a cluster of $M = 5 \times 10^{14} h^{-1} M_{\odot}$ ($\theta_{\text{vir}} = 3.0$) at $z_L = 1$. The top panels show the lensed temperature field (*left*) and the difference from the intrinsic temperature field (*right*). Gravitational lensing imprints dipole-like wiggles in the CMB map on top of the smooth large-scale gradient field. Perpendicular to the gradient direction there exists no temperature change and hence lensing reconstruction is degenerate along the direction. The bottom panels show the kSZ effect with $\Delta T_{\text{kSZ}} = 3 \mu\text{K}$ (*left*) and $15 \mu\text{K}$ (*right*). We assume that the cluster is moving toward the observer. With the small optical depth in the left panel, the kSZ effect is rel-

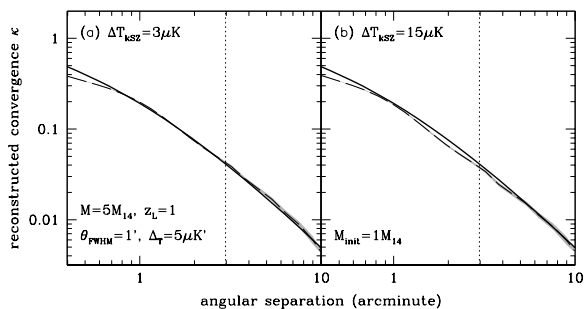


FIG. 8: Impact of kinetic Sunyaev-Zel'dovich (kSZ) effects on the mass profile reconstruction. Assuming that the gas distribution traces the dark matter distribution in clusters, the kSZ effect is computed by assigning a Gaussian random velocity to each cluster with rms temperature change $\Delta T_{\text{kSZ}} = 3$ (left) and $15 \mu\text{K}$ (right) at the center, respectively.

atively small compared to the lensing effect. Larger optical depth in the right panel substantially enhances the kSZ effect, dominating over the lensing effect at the center. However, since the lensing effect is much less concentrated than the kSZ effect as the dipole-like wiggles peak at a few scale radii (*top right*), the reconstruction is still possible.

Figure 8 shows the impact of the kSZ effect on reconstructing mass profiles. For clusters of $M = 5 \times 10^{14} h^{-1} M_{\odot}$ at $z_L = 1$ in an experiment with $\theta_{\text{FWHM}} = 1'$ and $\sigma_{\text{pix}} = 5 \mu\text{K}$, we iteratively use improved quadratic estimators with $M_{\text{init}} = 1 \times 10^{14} h^{-1} M_{\odot}$. The mean and the uncertainties are computed from 1000 clusters. Figure 8a shows that the kSZ effect with $\Delta T_{\text{kSZ}} = 3 \mu\text{K}$ has relatively little impact on the reconstruction: the kSZ effect becomes negligible beyond r_s because the density profile declines r^{-3} (the gas density in reality would be steeper and more confined to the center than we assumed here). The lensing effect, on the other hand, is sensitive to the deflection field and remains strong beyond r_s , declining less rapidly than the kSZ effect [29]. In Fig. 8b, we consider a larger kSZ effect with $\Delta T_{\text{kSZ}} = 15 \mu\text{K}$, expected either from higher electron number density or from higher matter fluctuation normalization $\sigma_8 \propto \sigma_v$. With the temperature anisotropies comparable to the lensing effect, the reconstruction becomes difficult and it starts to develop bias around R_{vir} as ΔT_{kSZ} increases. Note that the bias at the center is largely due to the telescope beam effect.

In the presence of contaminants such as residual foreground or tSZ effect, radio point sources, and large kSZ effect, the lensing estimators based on temperature anisotropies need to be complemented by using lensing estimators based on combination of temperature and E- and B-mode polarization [19], since there exists no significant source of contamination that mimics the intrinsic CMB polarization. Furthermore, the unique relation between the E- and B-mode polarization signals [36, 37] can be used to provide a robust consistency check. However, measurements of the lensed polarization fields would require an experiment with higher angular resolution and sensitive detectors than experiments that are currently available.

V. DISCUSSION

Weak gravitational lensing of the CMB gives rise to a deviation of the two-point correlation function of the CMB temperature anisotropies from otherwise statistically isotropic function. Quadratic estimators [11] have been widely used to reconstruct cluster mass profiles and large-scale structure by measuring the induced anisotropies in the two-point correlation function. We have shown that standard quadratic estimators become optimal in the limit of no lensing, saturating the Cramér-Rao bound, while they become progressively biased and sub-optimal as the lensing effect increases. Especially for clusters that can be found by the ongoing SZ surveys like ACT and SPT, the standard quadratic estimators start to be biased at $z_L \simeq 0.3$, and at higher redshift, where the lensing effect is larger, other estimators should be used to reconstruct cluster mass profiles.

It is recently proposed [14] that this obstacle in the standard quadratic estimators can be overcome by explicitly removing the signals in the CMB temperature gradient field at $l \geq l_{\text{cut}}$, where the lensing effect is large in violation of the linear approximation. However, although these modified quadratic estimators recover cluster mass profiles with no significant bias, the choice of l_{cut} is somewhat arbitrary and it depends on the lensing effect, which requires prior calibrations against numerical simulations before one can apply the modified quadratic estimators to CMB maps.

We have developed a new maximum likelihood estimator for reconstructing cluster mass profiles and large-scale structure. We first construct a CMB temperature field by delensing the observed temperature field based on an assumed mass model. We have proved that the delensed temperature field is close to the unlensed temperature field with telescope beam smoothed and detector noise added, if the assumed mass model is a good approximation to the true mass model. The delensed temperature field can then be used to set up the likelihood of the CMB, and our new estimator that maximizes this likelihood takes a similar form of the standard quadratic estimators, because it approaches to an optimal estimator as the assumed model becomes the true model. Our maximum likelihood estimator can be iteratively applied as we update the assumed mass model, until it converges (to the true model) and the estimate is consistent with the assumed model. Our maximum likelihood estimator, named as an improved quadratic estimator, is easy to implement in practice and it has no free parameter.

Our improved quadratic estimators quickly converge to the true mass model after a few iterations, even when an assumed initial model is significantly different from the true model. When the estimate is inconsistent with the assumed model, one can adopt another initial model for iterations for faster convergence of the improved quadratic estimators. The telescope beam and detector noise renders the reconstruction harder, but we have demonstrated that the improved quadratic estimators recover cluster mass profiles with a beam size comparable to the cluster scale radius. Furthermore, our new estimator significantly improves the signal-to-noise ratio over the standard or modified quadratic estimators by a factor of ten in

number of clusters, because when an assumed model is close to the true mass model, the only source of noise for our estimator is the intrinsic fluctuations of the CMB temperature gradient.

We have tested the robustness of the improved quadratic estimators in the presence of the kSZ effect. The kSZ distortion $\Delta T_{\text{kSZ}} \leq 15 \mu\text{K}$ at the center results in relatively small bias in the reconstructed cluster mass profiles. However, since the optical depth is a function of electron number density in the clusters, it is related to the true mass profile. Therefore, we could take a more aggressive approach to modeling kSZ signals from an assumed initial mass model and subtract the kSZ contributions before applying improved quadratic estimators. Furthermore, this template for kSZ signals can also be iteratively refined as we update our assumed mass model.

Since the reconstruction is non-parametric, it is not limited to spherical clusters, while stacking many clusters ensures that irregular shapes of individual clusters become irrelevant. Similar arguments can be applied to projection effects: each cluster can be located at a line-of-sight with overdense or underdense regions, but projection effects become negligible once many lines-of-sight are combined. Given a sample of clusters from SZ surveys, the average mass profile of stacked clusters would provide a cluster-mass cross-correlation function, which can be used to measure the growth rate of structure, probing the evolution of dark energy, instead of individual cluster mass profiles.

However, in reality it would be harder to reconstruct cluster mass profiles than considered here, because there exist other contaminants such as point radio sources and residual foreground and/or tSZ effect, and other complications such as non-isolated clusters and internal bulk motion of gas in clusters. However, additional information from polarization measurements may be used to overcome some of the difficulties, given the unique relation between the E- and B-mode polarization signals and relatively negligible primary and secondary contaminants. Finally we mention that our improved quadratic estimators can be applied to reconstruct large-scale structure, while in this regime standard quadratic estimators can be used without significant bias.

Acknowledgments

We thank Oliver Zahn for useful discussion. J. Y. thanks C. K. Chan for technical help on FFTw routines. J. Y. is supported by the Harvard College Observatory under the Donald H. Menzel fund. M. Z. is supported by the David and Lucile Packard, the Alfred P. Sloan, and the John D. and Catherine T. MacArthur Foundations. This work was further supported by NSF grant AST 05-06556 and NASA ATP grant NNG 05GJ40G.

APPENDIX A: DELENSED TEMPERATURE FIELD

Here we derive a relation $\hat{T}_1 \simeq T_1 e^{-\frac{1}{2}l^2\sigma_v^2} + T_1^N$ in the presence of telescope beam and detector noise. Given the

lensing potential $\phi^m(\hat{\mathbf{n}})$ of an assumed mass model, the lensing equation relates an image position $\hat{\mathbf{n}}$ to a source position $\hat{\mathbf{s}}^m = \hat{\mathbf{n}} + \hat{\nabla}\phi^m(\hat{\mathbf{n}})$. Here we keep the superscript m to indicate the relation to the assumed model. The true source position is then $\hat{\mathbf{s}} = \hat{\mathbf{n}} + \hat{\nabla}\phi(\hat{\mathbf{n}})$, where $\phi(\hat{\mathbf{n}})$ is the true lensing potential. Now we construct a delensed temperature field

$$\begin{aligned} \hat{T}(\hat{\mathbf{s}}^m) &= \tilde{T}^{\text{obs}}(\hat{\mathbf{n}}) \\ &= \int d^2\hat{\mathbf{m}} B(\hat{\mathbf{m}} - \hat{\mathbf{n}}) \tilde{T}(\hat{\mathbf{m}}) + T^N(\hat{\mathbf{n}}), \end{aligned} \quad (\text{A1})$$

where $B(\hat{\mathbf{m}})$ is the telescope beam function. Since the lensing equation is not analytically invertible in general, we keep both $\hat{\mathbf{s}}^m$ and $\hat{\mathbf{n}}$, but note that they are not independent variables. In Fourier space, the delensed temperature field is

$$\hat{T}_1 = \int d^2\hat{\mathbf{s}}^m \hat{T}(\hat{\mathbf{s}}^m) e^{-i\mathbf{l}\cdot\hat{\mathbf{s}}^m} \equiv \hat{T}_1^S + \hat{T}_1^N, \quad (\text{A2})$$

with a contribution from the CMB

$$\begin{aligned} \hat{T}_1^S &= \int d^2\hat{\mathbf{s}}^m \int d^2\hat{\mathbf{m}} B(\hat{\mathbf{m}} - \hat{\mathbf{n}}) \tilde{T}(\hat{\mathbf{m}}) e^{-i\mathbf{l}\cdot\hat{\mathbf{s}}^m} \\ &= \int d^2\mathbf{l}_1 B_{\mathbf{l}_1} \tilde{T}_{\mathbf{l}_1} \int \frac{d^2\hat{\mathbf{s}}^m}{(2\pi)^2} e^{i\mathbf{l}_1\cdot\hat{\mathbf{n}} - i\mathbf{l}\cdot\hat{\mathbf{s}}^m}, \end{aligned} \quad (\text{A3})$$

and a contribution from the detector noise

$$\begin{aligned} \hat{T}_1^N &= \int d^2\hat{\mathbf{s}}^m T^N(\hat{\mathbf{n}}) e^{-i\mathbf{l}\cdot\hat{\mathbf{s}}^m} \\ &= \int d^2\mathbf{l}_1 T_{\mathbf{l}_1}^N \int \frac{d^2\hat{\mathbf{s}}^m}{(2\pi)^2} e^{i\mathbf{l}_1\cdot\hat{\mathbf{n}} - i\mathbf{l}\cdot\hat{\mathbf{s}}^m}. \end{aligned} \quad (\text{A4})$$

The lensed temperature is $\tilde{T}(\hat{\mathbf{n}}) = T(\hat{\mathbf{s}})$ and its Fourier mode is

$$\tilde{T}_{\mathbf{l}} = \int d^2\mathbf{l}_1 T_{\mathbf{l}_1} \int \frac{d^2\hat{\mathbf{n}}}{(2\pi)^2} e^{-i\mathbf{l}\cdot\hat{\mathbf{n}} + i\mathbf{l}_1\cdot\hat{\mathbf{s}}}. \quad (\text{A5})$$

With the linear approximation, one can expand the exponential term to the first order in ϕ_1 and this equation reduces to Eq. (3). However, we keep the equation as general as possible to be valid, even when the lensing effect is large. Substituting $\tilde{T}_{\mathbf{l}_1}$ in Eq. (A3) and changing the integration variable $\hat{\mathbf{n}}$ to $\hat{\mathbf{s}}^m$ gives

$$\begin{aligned} \hat{T}_1^S &= \int d^2\mathbf{l}_1 \int d^2\mathbf{l}_2 B_{\mathbf{l}_1} T_{\mathbf{l}_2} \int \frac{d^2\hat{\mathbf{n}}}{(2\pi)^2} \int \frac{d^2\hat{\mathbf{n}}_2}{(2\pi)^2} \left| \frac{d^2\hat{\mathbf{s}}^m}{d\hat{\mathbf{n}}^2} \right| \\ &\times e^{i\mathbf{l}_1\cdot(\hat{\mathbf{n}} - \hat{\mathbf{n}}_2)} e^{i(\mathbf{l}_2\cdot\hat{\mathbf{n}}_2 - \mathbf{l}\cdot\hat{\mathbf{n}})} e^{i[\mathbf{l}_2\cdot\hat{\nabla}\phi(\hat{\mathbf{n}}_2) - \mathbf{l}\cdot\hat{\nabla}\phi^m(\hat{\mathbf{n}})]}. \end{aligned} \quad (\text{A6})$$

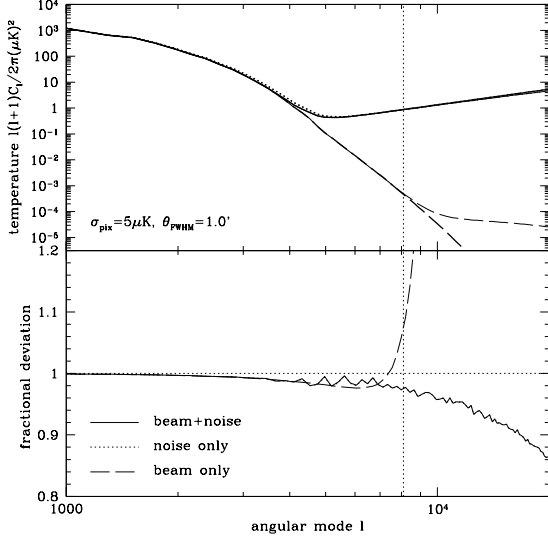


FIG. 9: Effects of telescope beam and detector noise on the delensing process. The top panel compares \hat{T}_1 (*thin*) with $T_1 e^{-\frac{1}{2}l^2\sigma_b^2} + T_1^N$ (*thick*) in terms of their power spectrum, and the bottom panel shows the fractional deviations. The vertical dotted line represents the beam scale $l = 1/\sigma_b$. CMB experiments with $\theta_{\text{FWHM}} = 1'$ and $\sigma_{\text{pix}} = 5\mu\text{K}$ are considered for clusters of $M = 5 \times 10^{14} h^{-1} M_\odot$ at $z_L = 1$. The noise only case is largely obscured by the solid line.

Given the lensing potential $\phi(\hat{\mathbf{n}})$ (analogously for $\phi^m(\hat{\mathbf{n}})$), the Jacobian is related to the distortion matrix

$$\left| \frac{d^2\hat{\mathbf{s}}}{d\hat{\mathbf{n}}^2} \right| = |\mathbf{M}^{-1}| = \left| \mathbf{I} + \hat{\nabla}\hat{\nabla}\phi \right| = \left| [1 - \kappa(\hat{\mathbf{n}})]^2 - \gamma^2(\hat{\mathbf{n}}) \right|, \quad (\text{A7})$$

and its inverse is the lensing magnification.

For a Gaussian beam $B_1 = \exp[-\frac{1}{2}l^2\sigma_b^2]$, we can integrate over the beam factor

$$\hat{T}_1^S = \int d^2\mathbf{l}_2 T_{\mathbf{l}_2} \int \frac{d^2\hat{\mathbf{n}}}{(2\pi)^2} \int \frac{d^2\hat{\mathbf{n}}_2}{(2\pi)^2} \left| \frac{d^2\hat{\mathbf{s}}^m}{d\hat{\mathbf{n}}^2} \right| \times \frac{2\pi}{\sigma_b^2} e^{-\frac{|\hat{\mathbf{n}}-\hat{\mathbf{n}}_2|^2}{2\sigma_b^2}} e^{i(\mathbf{l}_2 \cdot \hat{\mathbf{n}}_2 - \mathbf{l} \cdot \hat{\mathbf{n}})} e^{i[\mathbf{l}_2 \cdot \hat{\nabla}\phi(\hat{\mathbf{n}}_2) - \mathbf{l} \cdot \hat{\nabla}\phi^m(\hat{\mathbf{n}})]}. \quad (\text{A8})$$

Now we parametrize $\hat{\mathbf{n}}_2$ by a dimensionless displacement vector $\hat{\Delta}$ centered at $\hat{\mathbf{n}}$ (i.e., $\hat{\mathbf{n}}_2 = \hat{\mathbf{n}} + \sigma_b\hat{\Delta}$). The Gaussian beam factor guarantees that the integrand is non-vanishing only when $\Delta = |\hat{\Delta}|$ is small. In order to get more intuition, we expand $\phi(\hat{\mathbf{n}}_2) \simeq \phi(\hat{\mathbf{n}}) + \hat{\nabla}\phi(\hat{\mathbf{n}}) \cdot \sigma_b\hat{\Delta}$ to the linear order in Δ , and integrating over $\hat{\Delta}$ gives

$$\hat{T}_1^S = \int d^2\mathbf{l}_2 T_{\mathbf{l}_2} \int \frac{d^2\hat{\mathbf{n}}}{(2\pi)^2} \left| \frac{d^2\hat{\mathbf{s}}^m}{d\hat{\mathbf{n}}^2} \right| \quad (\text{A9})$$

$$\times e^{i(\mathbf{l}_2 \cdot \hat{\mathbf{s}} - \mathbf{l} \cdot \hat{\mathbf{s}}^m)} e^{-\frac{1}{2}\sigma_b^2 |\mathbf{M}^{-1} \cdot \mathbf{l}_2|^2}.$$

This is the final expression for the delensed temperature field. The first exponential term of the integrand controls the delensing process: when the assumed model is close to the true model after a few iterations ($\phi^m(\hat{\mathbf{n}}) \simeq \phi(\hat{\mathbf{n}})$, $\hat{\mathbf{s}}^m \simeq \hat{\mathbf{s}}$), the integral becomes a Dirac delta function and $\hat{T}_1^S = T_1$, when the beam smoothing is negligible. The distortion matrix is close to the identity matrix beyond R_{vir} and $\hat{T}_1^S \simeq T_1 e^{-\frac{1}{2}l^2\sigma_b^2}$. Around massive clusters, the distortion matrix deviates from the identity matrix and its determinant becomes smaller than one, making the exponential factor unity. This reflects that the beam size is reduced by a mapping from the image plane to the source plane, and practically $\hat{T}_1^S \simeq T_1 e^{-\frac{1}{2}l^2\tilde{\sigma}_b^2}$ with $\tilde{\sigma}_b < \sigma_b$.

For a white detector noise, the delensed detector noise is simply the redistributed white noise. However, since the delensing process alters the unit area on the sky, it becomes non-white but its deviation is confined to relatively small region; the noise power spectrum is

$$\begin{aligned} \langle \hat{T}_1^N \hat{T}_1^{N*} \rangle &= \int d^2\mathbf{l}_1 \int d^2\mathbf{l}_2 \langle T_{\mathbf{l}_1}^N T_{\mathbf{l}_2}^{N*} \rangle \\ &\times \int \frac{d^2\hat{\mathbf{s}}_1^m}{(2\pi)^2} \int \frac{d^2\hat{\mathbf{s}}_2^m}{(2\pi)^2} e^{i\mathbf{l}_1 \cdot \hat{\mathbf{n}}_1 - i\mathbf{l} \cdot \hat{\mathbf{s}}_1^m} e^{-i\mathbf{l}_2 \cdot \hat{\mathbf{n}}_2 + i\mathbf{l}' \cdot \hat{\mathbf{s}}_2^m} \\ &= C^N \int d^2\hat{\mathbf{s}}_1^m \int d^2\hat{\mathbf{s}}_2^m \delta(\hat{\mathbf{n}}_1 - \hat{\mathbf{n}}_2) e^{-i\mathbf{l} \cdot \hat{\mathbf{s}}_1^m + i\mathbf{l}' \cdot \hat{\mathbf{s}}_2^m} \\ &= C^N \int d^2\hat{\mathbf{s}}_1^m \left| \frac{d^2\hat{\mathbf{s}}_1^m}{d\hat{\mathbf{n}}_1^2} \right| e^{-i(1-1') \cdot \hat{\mathbf{s}}_1^m}. \quad (\text{A10}) \end{aligned}$$

It is the Jacobian of the distortion matrix that makes white noise non-white in a region around massive clusters. Outside R_{vir} , where the Jacobian is near unity, the integral becomes a Dirac delta function and the noise is again white.

Figure 9 compares our delensing (\hat{T}_1 : *thin*) and perfect delensing ($T_1 e^{-\frac{1}{2}l^2\sigma_b^2} + T_1^N$: *thick*) processes in terms of their power spectrum. In the absence of detector noise (*dashed*), \hat{T}_1^S starts to deviate from $T_1 e^{-\frac{1}{2}l^2\sigma_b^2}$ around the beam scale $l \simeq 1/\sigma_b$ (*vertical dotted*), declining less rapidly. On scales below the beam scale, our approximation ($\Delta \ll 1$) breaks down and $\mathbf{M}^{-1}(\hat{\mathbf{n}})$ differs from the identity matrix, leading to the excess power. However, at this scale, signals are dominated by the detector noise (*solid*). Since detector noises are unaffected by the beam distortion when delensed, the deviation of \hat{T}_1^N from T_1^N is relatively mild and it is solely due to the (inverse) magnification effect of the mapping from the image plane to the source plane. The noise only case (*dotted*) is largely obscured by the solid line. In summary, telescope beam and detector noise has little impact on our delensing process at scales larger than the beam scale, where most of the information is contained.

-
- [1] C. M. Hirata, N. Padmanabhan, U. Seljak, D. Schlegel, and J. Brinkmann, *Phys. Rev. D* **70**, 103501 (2004), arXiv:astro-ph/0406004.
- [2] K. M. Smith, O. Zahn, and O. Doré, *Phys. Rev. D* **76**, 043510 (2007), arXiv:0705.3980.
- [3] C. M. Hirata, S. Ho, N. Padmanabhan, U. Seljak, and N. Bahcall, ArXiv e-prints **801** (2008), 0801.0644.
- [4] E. Calabrese, A. Slosar, A. Melchiorri, G. F. Smoot, and O. Zahn, ArXiv e-prints **803** (2008), 0803.2309.
- [5] A. Albrecht et al., ArXiv Astrophysics e-prints (2006), astro-ph/0609591.
- [6] W. Hu, D. E. Holz, and C. Vale, *Phys. Rev. D* **76**, 127301 (2007), arXiv:0708.4391.
- [7] J. Silk, *Astrophys. J. Lett.* **151**, L19+ (1968).
- [8] U. Seljak and M. Zaldarriaga, *Astrophys. J.* **538**, 57 (2000), arXiv:astro-ph/9907254.
- [9] C. Vale, A. Amblard, and M. White, *New Astronomy* **10**, 1 (2004), arXiv:astro-ph/0402004.
- [10] G. Holder and A. Kosowsky, *Astrophys. J.* **616**, 8 (2004), arXiv:astro-ph/0401519.
- [11] W. Hu, *Astrophys. J. Lett.* **557**, L79 (2001), arXiv:astro-ph/0105424.
- [12] C. M. Hirata and U. Seljak, *Phys. Rev. D* **67**, 043001 (2003), arXiv:astro-ph/0209489.
- [13] M. Maturi, M. Bartelmann, M. Meneghetti, and L. Moscardini, *Astron. Astrophys.* **436**, 37 (2005), arXiv:astro-ph/0408064.
- [14] W. Hu, S. DeDeo, and C. Vale, *New Journal of Physics* **9**, 441 (2007), arXiv:astro-ph/0701276.
- [15] M. Tegmark and et al., *Phys. Rev. D* **74**, 123507 (2006), arXiv:astro-ph/0608632.
- [16] D. N. Spergel and et al., *Astrophys. J. Suppl. Ser.* **170**, 377 (2007), arXiv:astro-ph/0603449.
- [17] E. Komatsu and et al., ArXiv e-prints **803** (2008), 0803.0547.
- [18] W. Hu, *Phys. Rev. D* **62**, 043007 (2000), arXiv:astro-ph/0001303.
- [19] T. Okamoto and W. Hu, *Phys. Rev. D* **67**, 083002 (2003), arXiv:astro-ph/0301031.
- [20] A. Challinor and A. Lewis, *Phys. Rev. D* **71**, 103010 (2005), arXiv:astro-ph/0502425.
- [21] K. S. Mandel and M. Zaldarriaga, *Astrophys. J.* **647**, 719 (2006), arXiv:astro-ph/0512218.
- [22] A. Lewis and A. Challinor, *Phys. Rep.* **429**, 1 (2006), arXiv:astro-ph/0601594.
- [23] L. Knox, *Phys. Rev. D* **52**, 4307 (1995), arXiv:astro-ph/9504054.
- [24] O. Zahn and M. Zaldarriaga, *Astrophys. J.* **653**, 922 (2006), arXiv:astro-ph/0511547.
- [25] D. Babich, *Phys. Rev. D* **72**, 043003 (2005), arXiv:astro-ph/0503375.
- [26] J. F. Navarro, C. S. Frenk, and S. D. M. White, *Astrophys. J.* **490**, 493 (1997), astro-ph/9611107.
- [27] M. Bartelmann, *Astron. Astrophys.* **313**, 697 (1996), arXiv:astro-ph/9602053.
- [28] C. O. Wright and T. G. Brainerd, *Astrophys. J.* **534**, 34 (2000).
- [29] U. Seljak and M. Zaldarriaga, *Astrophys. J.* **469**, 437 (1996), astro-ph/9603033.
- [30] R. A. Sunyaev and Y. B. Zeldovich, *Comments on Astrophysics and Space Physics* **2**, 66 (1970).
- [31] R. A. Sunyaev and Y. B. Zeldovich, *Comments on Astrophysics and Space Physics* **4**, 173 (1972).
- [32] S. Dodelson, *Phys. Rev. D* **70**, 023009 (2004), arXiv:astro-ph/0402314.
- [33] A. Lewis and L. King, *Phys. Rev. D* **73**, 063006 (2006), arXiv:astro-ph/0512104.
- [34] M. Birkinshaw, *Phys. Rep.* **310**, 97 (1999), arXiv:astro-ph/9808050.
- [35] J. E. Carlstrom, G. P. Holder, and E. D. Reese, *Annu. Rev. Astron. Astrophys.* **40**, 643 (2002), arXiv:astro-ph/0208192.
- [36] U. Seljak and M. Zaldarriaga, *Phys. Rev. Lett.* **78**, 2054 (1997), arXiv:astro-ph/9609169.
- [37] M. Kamionkowski, A. Kosowsky, and A. Stebbins, *Phys. Rev. Lett.* **78**, 2058 (1997), arXiv:astro-ph/9609132.